

GOODS-ALMA 2.0: Starbursts in the main sequence reveal compact star formation regulating galaxy evolution prequenching

C. Gómez-Guijarro¹, D. Elbaz¹, M. Xiao^{1,2}, V. I. Kokorev^{3,4}, G. E. Magdis^{3,5,4}, B. Magnelli¹, E. Daddi¹, F. Valentino^{3,4}, M. T. Sargent^{6,7}, M. Dickinson⁸, M. Béthermin⁹, M. Franco¹⁰, A. Pope¹¹, B. S. Kalita¹, L. Ciesla⁹, R. Demarco¹², H. Inami¹³, W. Rujopakarn^{14,15,16}, X. Shu¹⁷, T. Wang², L. Zhou^{2,18}, D. M. Alexander¹⁹, F. Bournaud¹, R. Chary²⁰, H. C. Ferguson²¹, S. L. Finkelstein²², M. Giavalisco¹¹, D. Iono^{23,24}, S. Juneau⁸, J. S. Kartaltepe²⁵, G. Lagache⁹, E. Le Floc'h¹, R. Leiton¹², L. Leroy¹, L. Lin²⁶, K. Motohara²⁷, J. Mullaney²⁸, K. Okumura¹, M. Pannella^{29,30}, C. Papovich^{31,32}, and E. Treister³³

(Affiliations can be found after the references)

Received 1 October 2021 / Accepted 16 December 2021

ABSTRACT

Compact star formation appears to be generally common in dusty star-forming galaxies (SFGs). However, its role in the framework set by the scaling relations in galaxy evolution remains to be understood. In this work we follow up on the galaxy sample from the GOODS-ALMA 2.0 survey, an ALMA blind survey at 1.1 mm covering a continuous area of 72.42 arcmin² using two array configurations. We derived physical properties, such as star formation rates, gas fractions, depletion timescales, and dust temperatures for the galaxy sample built from the survey. There exists a subset of galaxies that exhibit starburst-like short depletion timescales, but they are located within the scatter of the so-called main sequence of SFGs. These are dubbed starbursts in the main sequence and display the most compact star formation and they are characterized by the shortest depletion timescales, lowest gas fractions, and highest dust temperatures of the galaxy sample, compared to typical SFGs at the same stellar mass and redshift. They are also very massive, accounting for ~60% of the most massive galaxies in the sample ($\log(M_*/M_\odot) > 11.0$). We find trends between the areas of the ongoing star formation regions and the derived physical properties for the sample, unveiling the role of compact star formation as a physical driver of these properties. Starbursts in the main sequence appear to be the extreme cases of these trends. We discuss possible scenarios of galaxy evolution to explain the results drawn from our galaxy sample. Our findings suggest that the star formation rate is sustained in SFGs by gas and star formation compression, keeping them within the main sequence even when their gas fractions are low and they are presumably on the way to quiescence.

Key words. galaxies: evolution – galaxies: fundamental parameters – galaxies: high-redshift – galaxies: star formation – galaxies: structure – submillimeter: galaxies

1. Introduction

The cosmic history of stellar mass assembly in galaxy evolution is directly linked with the star formation history. The cosmic star formation rate (SFR) density manifests a gradual growth from the epochs of formation of the first galaxies until it peaks at $z \sim 2$, followed by a factor 10 decline until $z \sim 0$ (see Madau & Dickinson 2014, for a review).

Numerous studies revealed the existence of a tight correlation between the SFR and the stellar mass of star-forming galaxies (SFGs), the so-called main sequence (MS) of SFGs (e.g., Brinchmann et al. 2004; Daddi et al. 2007; Elbaz et al. 2007; Noeske et al. 2007; Whitaker et al. 2012). The MS shows signs of a small scatter at least up to $z \sim 4$ (~ 0.3 dex; e.g., Elbaz et al. 2007; Noeske et al. 2007; Whitaker et al. 2012; Speagle et al. 2014; Schreiber et al. 2015), which suggests that secular evolution is the dominant mode of stellar assembly, involving a steady equilibrium between gas inflows, outflows, and consumption in star formation (e.g., Daddi et al. 2010; Tacconi et al. 2010; Genzel et al. 2010; Dekel et al. 2013; Feldmann & Mayer 2015). The average SFR at a fixed stellar mass is higher with increasing redshift, which is reflected in the rise of the MS normalization with increasing redshift (e.g., Noeske et al. 2007; Whitaker et al. 2012; Speagle et al. 2014; Schreiber et al. 2015; Leslie et al. 2020). Outliers to the MS exist at all redshifts char-

acterized by their elevated SFR compared to MS galaxies at a fixed stellar mass and redshift. Galaxies of this kind are commonly referred to as starbursts galaxies (SBs). In addition to the latter, various other definitions of SBs are widespread in the literature (see Heckman 2005, for a compilation). Particularly important for this work are the definitions of SBs of an anomalously rapid gas consumption reflected in short depletion timescales compared to normal SFGs at a fixed stellar mass and redshift, as well as the definition based on the elevated SFR compared to MS galaxies at a fixed stellar mass and redshift.

Understanding the evolution of the SFR density and the secular mode of stellar mass assembly implied by the MS requires one to study the cold gas reservoirs that fuel star formation. Investigation of the evolution of the cold gas density has uncovered that it closely follows the evolution of the SFR density (e.g., Riechers et al. 2019; Decarli et al. 2019; Magnelli et al. 2020). In the last decade, numerous studies have progressively revealed the increase in the gas content and decrease in the depletion timescales with increasing redshift (e.g., Daddi et al. 2008, 2010; Tacconi et al. 2010; Genzel et al. 2010; Magdis et al. 2012; Béthermin et al. 2015; Dessauges-Zavadsky et al. 2020; Donevski et al. 2020; Kokorev et al. 2021). More recently, large statistical galaxy samples have established the gas scaling relations for the gas fractions ($f_{\text{gas}} = M_{\text{gas}}/(M_{\text{gas}} + M_*)$) and depletion timescales ($\tau_{\text{dep}} = M_{\text{gas}}/\text{SFR}$), with their dependencies

on a specific star formation rate ($sSFR = SFR/M_*$), stellar mass, as well as lookback time (e.g., [Scoville et al. 2017](#); [Tacconi et al. 2018](#); [Liu et al. 2019](#)). The overall larger amount of gas looks to be the main responsible factor for the average increase in the SFR with increasing redshift, while at a fixed stellar mass and redshift, both a mix of higher gas fractions and lower depletion timescales are invoked to explain the existence of SBs.

Gas appears to be the main regulator of galaxy evolution and galaxy growth seems to be a relatively smooth process over long timescales, as shown by the gas evolution dominating the behavior of the cosmic SFR density and the existence of the MS. Self-regulation seems to be typical among galaxies, as only a minor fraction of SFGs deviate from the equilibrium, normally associated with disruptive dynamical events, such as galaxy mergers (e.g., [Joseph & Wright 1985](#); [Kartaltepe et al. 2012](#); [Cibinel et al. 2019](#)). An always increasing number of galaxies fall off the MS when the star formation shuts off or drastically decreases (e.g., [Brammer et al. 2011](#); [Straatman et al. 2015](#); [Davidzon et al. 2017](#)), which is the so-called quenching of star formation that leads to the formation of quiescent galaxies (QGs).

However, the detailed mechanisms governing the overall smooth and self-regulated galaxy evolution set by the gas scaling relations and the MS framework remain to be understood. The study of the properties of SFGs, especially those within the scatter of the MS, offers the means to explore these mechanisms further. In the last years, the Atacama Large Millimeter/submillimeter array (ALMA) has opened new frontiers (see [Hodge & da Cunha 2020](#), for a review). A number of studies have indicated that star formation traced by submm/mm dust continuum emission takes place in compact areas smaller than the stellar sizes (e.g., [Simpson et al. 2015](#); [Ikarashi et al. 2015](#); [Hodge et al. 2016](#); [Fujimoto et al. 2017, 2018](#); [Gómez-Guijarro et al. 2018, 2022](#); [Elbaz et al. 2018](#); [Lang et al. 2019](#); [Rujopakarn et al. 2019](#); [Gullberg et al. 2019](#); [Franco et al. 2020a](#)). Similar results have been also found in radio emission (e.g., [Murphy et al. 2017](#); [Jiménez-Andrade et al. 2019, 2021](#)). Furthermore, other recent works have discovered the existence of a population of SBs within the scatter of the MS, owing to their short depletion timescales and enhanced star formation surface densities, exhibiting compact star formation traced by submm/mm dust continuum emission ([Elbaz et al. 2018](#)) or, similarly, compact radio emission ([Jiménez-Andrade et al. 2019](#)). Besides, a population of galaxies within the scatter of the MS displayed compact star formation as traced by CO lines ([Puglisi et al. 2019](#)).

Nevertheless, the role of compact star formation and of the population of SBs in the MS in the more general smooth and self-regulated galaxy growth is yet to be comprehended. Several studies have advocated for compaction events predicted by galaxy formation models in which extended SFGs in the MS can secularly evolve into compact SFGs in the MS by funneling gas to their central regions yielding the build up of their stellar cores (e.g., [Dekel et al. 2013](#); [Zolotov et al. 2015](#); [Tacchella et al. 2016](#)). Other studies have advocated that SBs dominated by a violent episode of star formation typical of gas-rich mergers that move well above the scatter of the MS are also capable of funneling gas to the center of collision and quickly build up compact stellar cores (e.g., [Mihos & Hernquist 1996](#); [Hopkins et al. 2006](#); [Toft et al. 2014](#); [Gómez-Guijarro et al. 2018](#); [Puglisi et al. 2021](#)). In the latter scenario compact SFGs in the MS would be fading SBs where most of the gas has already been consumed, located within the scatter of the MS, but on their way to

quiescence (e.g., [Elbaz et al. 2018](#); [Gómez-Guijarro et al. 2019](#); [Puglisi et al. 2021](#)).

In this work, we aim at studying these unknowns about the role of compact star formation and the origin, nature, and role of SBs in the MS in galaxy evolution. We follow up on the galaxy sample presented in [Gómez-Guijarro et al. \(2022\)](#) from the GOODS-ALMA 2.0 survey, an ALMA blind survey at 1.1 mm covering a continuous area of 72.42 arcmin² using two array configurations at a similar and homogeneous depth over the whole field. The combined mosaic with both configurations reaches an average sensitivity of 68.4 $\mu\text{Jy beam}^{-1}$ at an average angular resolution of $0''.447 \times 0''.418$. The layout of the paper is as follows. An overview of the GOODS-ALMA survey, galaxy sample, and multiwavelength ancillary data involved in this work is given in Sect. 2. In Sect. 3 we present the dust and stellar-based properties of the galaxy sample. Section 4 is dedicated to study the physical properties of the galaxy sample in the framework of the MS and the scaling relations for depletion timescales, gas fractions, and dust temperatures. We investigate the role of compact star formation, traced by the dust continuum emission, as a physical driver of the galaxy sample behavior in relation with the scaling relations in Sect. 5. In Sect. 6 we discuss and interpret our results in the broader cosmological context along with literature studies. We summarize the main findings and conclusions in Sect. 7.

Throughout this work we adopt a concordance cosmology $[\Omega_\Lambda, \Omega_M, h] = [0.7, 0.3, 0.7]$ and a Salpeter initial mass function (IMF; [Salpeter 1955](#)). When magnitudes are quoted they are in the AB system ([Oke 1974](#)).

2. Sample and data

2.1. ALMA 1.1 mm galaxy survey in GOODS-South

GOODS-ALMA is a 1.1 mm galaxy survey in the Great Observatories Origins Deep Survey South field (GOODS-South; [Dickinson et al. 2003](#); [Giavalisco et al. 2004](#)) carried out with ALMA Band 6. GOODS-ALMA extends over a continuous area of 72.42 arcmin² (primary beam response level $\geq 20\%$) centered at $\alpha = 3^{\text{h}}32^{\text{m}}30^{\text{s}}$, $\delta = -27^{\circ}48'00''$ with a homogeneous average sensitivity employing two different array configurations: Cycle 3 observations (program 2015.1.00543.S; PI: D. Elbaz) provided the high-resolution small spatial scales using a more extended array configuration (high resolution dataset), while Cycle 5 observations (program 2017.1.00755.S; PI: D. Elbaz) provided the low-resolution large spatial scales employing a more compact array configuration (low resolution dataset). The high resolution dataset was presented in [Franco et al. \(2018\)](#) (GOODS-ALMA 1.0). The low resolution dataset and its combination with the high resolution (combined dataset) was presented in [Gómez-Guijarro et al. \(2022\)](#); (GOODS-ALMA 2.0), improving the uv coverage and sensitivity. On average, the high resolution and low resolution mosaics have similar sensitivities of 89.0 and 95.2 $\mu\text{Jy beam}^{-1}$ at an angular resolution of $0''.251 \times 0''.232$ and $1''.33 \times 0''.935$, respectively (synthesized beam FWHM along the major \times minor axis). The combined mosaic reaches an average sensitivity of 68.4 $\mu\text{Jy beam}^{-1}$ at an average angular resolution of $0''.447 \times 0''.418$.

In this work, we used the GOODS-ALMA 2.0 source catalog presented in [Gómez-Guijarro et al. \(2022\)](#), a sample composed of 88 sources, 50% detected at $S/N_{\text{peak}} \geq 5$ (sources detected with a purity of 100% associated with the absence of negative detections at the same significance) and 50% detected at $3.5 \leq S/N_{\text{peak}} \leq 5$ aided by priors. We refer the reader to

Gómez-Guijarro et al. (2022) for further details about the observations, data processing, source catalog, and 1.1 mm flux density and size measurements.

2.2. Multiwavelength ancillary data

Ultraviolet (UV) to near-infrared (near-IR) data were taken from the K_s -band-selected ZFOURGE catalog by Straatman et al. (2016). ZFOURGE (PI: I. Labbé) uses five near-IR medium bands (J_1 , J_2 , J_3 , H_s , and H_l) and the K_s -band. It combines dedicated FourStar/ K_s -band observations with preexisting K -band imaging to create super-deep detection images: in the CDFS field (containing GOODS-South) VLT/HAWK-I/ K from HUGS (Fontana et al. 2014), VLT/ISAAC/ K from GOODS, ultra deep data in the HUDF region (Retzlaff et al. 2010), CFHST/WIRCAM/ K from TENIS (Hsieh et al. 2012), and Magellan/PANIC/ K in HUDF (PI: I. Labbé). The ancillary CDFS UV to near-IR filters include VLT/VIMOS/ U , R -imaging (Nonino et al. 2009), HST/ACS/ B , V , I , Z -imaging (Giavalisco et al. 2004; Wuyts et al. 2008), ESO/MPG/WFI/ U_{38} , V , R_c -imaging (Erben et al. 2005; Hildebrandt et al. 2006), HST/WFC3/ $F098M$, $F105W$, $F125W$, $F140W$, $F160W$ and HST/ACS/ $F606W$, $F814W$ -imaging (Grogin et al. 2011; Koekemoer et al. 2011; Windhorst et al. 2011; Brammer et al. 2012), and 11 Subaru/Suprime-Cam optical medium bands (Cardamone et al. 2010). *Spitzer*/IRAC/3.6 and 4.5 μm images are the ultra-deep mosaics from the IUDF (Labbé et al. 2015), using data from the IUDF (PI: I. Labbé) and IGOODS (PI: P. Oesch) programs, combined with GOODS (PI: M. Dickinson), ERS (PI: G. Fazio), S-CANDELS (PI: G. Fazio), SEDS (PI: G. Fazio), and UDF2 (PI: R. Bouwens). Mid-IR *Spitzer*/IRAC/5.8 and 8.0 μm images are from GOODS (PI: M. Dickinson).

Additionally, we used mid-IR to submm data including *Spitzer*/MIPS/24 μm images from GOODS (PI: M. Dickinson), *Herschel*/PACS/70, 100, 160 μm from GOODS-*Herschel* (Elbaz et al. 2011, PI: D. Elbaz) and PEP (Lutz et al. 2011) combined (Magnelli et al. 2013), and *Herschel*/SPIRE/250, 350, 500 μm from HerMES (Oliver et al. 2012). In radio, VLA observations in GOODS-South (PI: W. Rujopakarn) were taken at 3 GHz (10 cm) covering the entire GOODS-ALMA field (Rujopakarn et al., in prep.) and at 6 GHz (5 cm) around the HUDF with partial coverage of GOODS-ALMA (Rujopakarn et al. 2016). For the *Herschel* data, the PACS PEP/GOODS-*Herschel* reach 3σ depths of 0.9, 0.6, and 1.3 mJy at 70, 100, 160 μm , respectively (Magnelli et al. 2013). The SPIRE HerMES reach 5σ depths of 4.3, 3.6, and 5.2 mJy at 250, 350, 500 μm , respectively (Oliver et al. 2012). In the case of SPIRE, its large beam yields a high confusion limit, requiring tailored de-blending methodologies to provide fluxes from the highly confused low-resolution data to optical counterparts. We used a catalog (T. Wang, priv. comm.) built using a state-of-the-art de-blending methodology similar to that applied in the “super-deblended” catalogs in the GOODS-North (Liu et al. 2018) and COSMOS (Jin et al. 2018) fields. Briefly, source extraction was run on the SPIRE images starting with all the MIPS 24 μm priors down to 20 μJy . This flux level yielded a prior density of ~ 1 source/beam, which maximized the efficiency of source extraction. A first PSF-fitting run determined flux densities and uncertainties. After that, a second run was performed by freezing faint sources to their predicted fluxes if they had a brighter neighbor within 1.5 pixels. Flux measurements were crossed checked with those predicted from spectral energy distribution (SED) fitting to the mid-IR to submm data. Overall, this methodology helps to break

blending degeneracies in crowded regions, yielding $\times 2$ –10 lower RMS levels and more accurate flux density measurements for the majority of nonfrozen sources and cleaner residual images.

3. Dust and stellar-based properties

3.1. Redshifts and stellar masses

The redshifts and stellar masses for the 88 ALMA sources that compose our galaxy sample were presented in Gómez-Guijarro et al. (2022). These values are recapitulated in Tables 1 and 2. In summary, we searched for stellar counterparts in the ZFOURGE catalog by Straatman et al. (2016), which provides photometric redshift and stellar mass estimations. Spectroscopic redshifts were obtained through a recent compilation in GOODS-South (N. Hathi, priv. comm.), along with additional recent surveys in the field: VANDELS (Garilli et al. 2021), the MUSE-Wide survey (Herenz et al. 2017; Urrutia et al. 2019), and ASPECS LP (Decarli et al. 2019; González-López et al. 2019; Boogaard et al. 2019) (see Gómez-Guijarro et al. 2022, for the spectroscopic redshift references therein). When the redshifts were updated by new spectroscopic values compared to the photometric redshifts from ZFOURGE, the stellar mass estimations were updated employing the same methodology as ZFOURGE: photometry was fit using FAST++¹, an updated version of the SED fitting code FAST (Kriek et al. 2009) employed in ZFOURGE. The stellar population models were from Bruzual & Charlot (2003), with exponentially declining star formation histories, Calzetti et al. (2000) dust attenuation law, and fixed solar metallicity. The stellar masses were multiplied by a factor of 1.7 to scale them from a Chabrier (Chabrier 2003) to a Salpeter (Salpeter 1955) IMF (e.g., Reddy et al. 2006; Santini et al. 2012; Elbaz et al. 2018). In addition, the redshifts and stellar masses of the six optically dark galaxies in Zhou et al. (2020), namely AGS4, AGS11, AGS15, AGS17, AGS24, and AGS25 (A2GS2, A2GS15, A2GS10, A2GS7, A2GS29, and A2GS17, respectively), were substituted by the values in that work, where they were studied in detail. Tailored photometry was obtained for four galaxies that were affected by blending (A2GS28, A2SGS30, A2GS33, and A2GS60) and for an extra galaxy with no counterpart in the ZFOURGE catalog (A2GS38), employing updated HST data from the HLF-GOODS-S v2.0 mosaics (Illingworth et al. 2016; Whitaker et al. 2019) homogenized to the WFC3/ $F160W$ -band PSF, along with the ground-based bands in ZFOURGE homogenized to a common Moffat PSF profile (0'9 FWHM; see Straatman et al. 2016), and the *Spitzer*/IRAC data. The photometry was carried out following the methodology described in Gómez-Guijarro et al. (2018) for crowded and blended sources: all the bands affected by blending were fit using GALFIT (Peng et al. 2002), with priors set to the number of sources in the $F160W$ -band image. For the bands unaffected by blending, aperture photometry was performed using aperture diameters of 0'7 for HST (as in Whitaker et al. 2019) and 1'2 for the ground-based data (as in Straatman et al. 2016) with aperture corrections to account for the flux losses outside the aperture. PSF photometry with GALFIT was used for the *Spitzer*/IRAC bands. Uncertainties were derived from empty aperture measurements.

¹ <https://github.com/cschreib/fastpp>

Table 1. Dust and stellar-based properties.

ID	z	$\log(M_*/M_\odot)$	$\log(L_{\text{IR}}/L_\odot)$	SFR ($M_\odot \text{ yr}^{-1}$)	ΔMS	$\log(M_{\text{dust}}/M_\odot)$	T_{dust} (K)	$\log(M_{\text{gas}}/M_\odot)$	f_{gas}	τ_{dep} (Myr)
(1)	(2)	(3)	(4)	(5)	(6)	(7)	(8)	(9)	(10)	(11)
A2GS1	2.309	11.06	12.80 ± 0.01	1093 ± 10	5.59 ± 0.05	9.03 ± 0.01	42.4 ^{+0.2} _{-0.2}	11.09 ± 0.20	0.52 ± 0.11	112 ± 51
A2GS2	3.556	11.09	12.92 ± 0.01	1428 ± 31	3.79 ± 0.08	8.93 ± 0.01	45.0 ^{+1.0} _{-0.5}	11.07 ± 0.20	0.49 ± 0.11	82 ± 37
A2GS3 ^(†)	2.582	11.44	12.86 ± 0.01	1251 ± 13	2.96 ± 0.03	9.03 ± 0.01	44.1 ^{+0.3} _{-0.3}	11.03 ± 0.20	0.28 ± 0.09	85 ± 39
A2GS4	2.918	10.76	12.92 ± 0.01	1416 ± 24	10.03 ± 0.17	8.97 ± 0.01	46.0 ^{+0.4} _{-0.3}	11.17 ± 0.20	0.72 ± 0.09	103 ± 47
A2GS5	1.797	11.09	12.55 ± 0.01	614 ± 11	4.37 ± 0.08	9.44 ± 0.01	32.8 ^{+0.2} _{-0.2}	11.45 ± 0.20	0.70 ± 0.10	460 ± 210
A2GS6	3.46	11.14	12.88 ± 0.01	1312 ± 29	3.25 ± 0.07	8.93 ± 0.01	45.6 ^{+1.2} _{-0.5}	11.05 ± 0.20	0.45 ± 0.11	85 ± 39
A2GS7	3.467	10.52	13.00 ± 0.03	1750 ± 100	17.7 ± 1.0	8.95 ± 0.03	(...)	11.28 ± 0.20	0.85 ± 0.06	108 ± 50
A2GS8 ^(*)	3.29	11.44	12.59 ± 0.04	665 ± 57	1.02 ± 0.09	8.91 ± 0.04	(...)	10.95 ± 0.20	0.24 ± 0.09	133 ± 63
A2GS9	2.696	10.90	12.30 ± 0.03	345 ± 22	1.95 ± 0.12	8.92 ± 0.03	31.3 ^{+4.6} _{-2.4}	11.06 ± 0.20	0.59 ± 0.11	330 ± 150
A2GS10 ^(*)	3.47	10.56	12.91 ± 0.03	1415 ± 85	13.03 ± 0.78	8.86 ± 0.03	(...)	11.18 ± 0.20	0.80 ± 0.07	106 ± 49
A2GS11 ^(†)	2.41	11.33	12.61 ± 0.01	694 ± 13	2.16 ± 0.04	9.05 ± 0.01	39.7 ^{+0.3} _{-0.3}	11.06 ± 0.20	0.35 ± 0.10	165 ± 76
A2GS12	3.847	10.87	12.62 ± 0.03	724 ± 52	2.89 ± 0.21	8.83 ± 0.03	(...)	11.05 ± 0.20	0.60 ± 0.11	156 ± 73
A2GS13	1.619	10.96	12.48 ± 0.01	521 ± 3	5.27 ± 0.03	9.18 ± 0.01	34.4 ^{+0.2} _{-0.2}	11.19 ± 0.20	0.63 ± 0.11	300 ± 140
A2GS14	1.956	11.19	12.32 ± 0.01	361 ± 4	1.95 ± 0.02	8.97 ± 0.01	36.3 ^{+0.1} _{-0.3}	10.97 ± 0.20	0.38 ± 0.11	260 ± 120
A2GS15	3.47	10.24	12.36 ± 0.02	391 ± 22	7.53 ± 0.42	8.81 ± 0.02	39.2 ^{+0.2} _{-1.7}	11.25 ± 0.20	0.91 ± 0.04	460 ± 210
A2GS16 ^(†)	2.45	11.39	12.33 ± 0.03	364 ± 21	1.01 ± 0.06	8.69 ± 0.03	40.7 ^{+1.1} _{-0.9}	10.69 ± 0.20	0.17 ± 0.06	130 ± 62
A2GS17 ^(*)	4.64	10.39	12.84 ± 0.04	1200 ± 110	11.5 ± 1.1	8.54 ± 0.04	(...)	11.00 ± 0.20	0.80 ± 0.07	84 ± 40
A2GS18 ^(*)	3.689	10.56	12.63 ± 0.05	738 ± 79	6.33 ± 0.68	8.52 ± 0.05	(...)	10.85 ± 0.20	0.66 ± 0.10	96 ± 46
A2GS19 ^(†)	2.225	11.43	12.39 ± 0.01	427 ± 10	1.35 ± 0.03	8.60 ± 0.01	43.4 ^{+0.6} _{-0.7}	10.57 ± 0.20	0.12 ± 0.05	85 ± 39
A2GS20	2.68	10.72	11.96 ± 0.04	157 ± 13	1.34 ± 0.11	9.20 ± 0.04	(...)	11.39 ± 0.20	0.82 ± 0.07	1540 ± 730
A2GS21	2.698	10.30	12.57 ± 0.01	639 ± 19	14.24 ± 0.43	8.89 ± 0.01	37.1 ^{+1.6} _{-0.7}	11.22 ± 0.20	0.90 ± 0.04	260 ± 120
A2GS22	2.72	10.77	12.22 ± 0.02	286 ± 14	2.14 ± 0.11	8.90 ± 0.02	35.4 ^{+1.0} _{-1.8}	11.07 ± 0.20	0.67 ± 0.10	410 ± 190
A2GS23	2.00	10.76	12.25 ± 0.01	306 ± 8	3.33 ± 0.09	8.97 ± 0.01	35.3 ^{+2.9} _{-1.4}	11.08 ± 0.20	0.67 ± 0.10	390 ± 180
A2GS24	2.32	11.38	12.33 ± 0.01	364 ± 12	1.13 ± 0.04	9.13 ± 0.01	36.0 ^{+0.9} _{-0.4}	11.12 ± 0.20	0.35 ± 0.10	360 ± 160
A2GS25	2.543	10.13	12.81 ± 0.01	1099 ± 11	38.65 ± 0.39	8.82 ± 0.01	48.9 ^{+0.5} _{-0.5}	11.21 ± 0.20	0.92 ± 0.03	145 ± 66
A2GS26	1.927	10.64	11.55 ± 0.04	61 ± 6	0.89 ± 0.09	9.22 ± 0.04	(...)	11.36 ± 0.20	0.84 ± 0.06	3700 ± 1800
A2GS27 ^(*)	4.72	11.01	12.39 ± 0.08	426 ± 77	0.96 ± 0.17	8.39 ± 0.08	(...)	10.61 ± 0.21	0.29 ± 0.10	96 ± 50
A2GS28	1.967	10.71	12.22 ± 0.02	283 ± 10	3.48 ± 0.12	8.60 ± 0.02	38.1 ^{+0.9} _{-0.8}	10.72 ± 0.20	0.50 ± 0.11	183 ± 84
A2GS29 ^(*)	3.47	11.32	12.40 ± 0.05	436 ± 54	0.75 ± 0.09	8.69 ± 0.05	(...)	10.76 ± 0.21	0.22 ± 0.08	131 ± 64
A2GS30 ^(†)	3.80	11.46	12.81 ± 0.01	1099 ± 37	1.28 ± 0.04	8.75 ± 0.01	59.1 ^{+1.5} _{-1.6}	10.81 ± 0.20	0.18 ± 0.07	58 ± 27
A2GS31 ^(†)	2.15	11.18	12.27 ± 0.01	322 ± 8	1.51 ± 0.04	8.77 ± 0.01	38.1 ^{+0.9} _{-0.8}	10.79 ± 0.20	0.29 ± 0.09	188 ± 86
A2GS32 ^(†)	2.251	11.55	12.39 ± 0.02	426 ± 20	1.15 ± 0.05	8.95 ± 0.02	36.8 ^{+0.9} _{-0.5}	10.90 ± 0.20	0.18 ± 0.07	188 ± 86
A2GS33 ^(*)	(...)	(...)	(...)	(...)	(...)	(...)	(...)	(...)	(...)	(...)
A2GS34 ^(†)	1.613	11.43	12.00 ± 0.01	170 ± 4	0.98 ± 0.02	8.84 ± 0.01	33.0 ^{+0.7} _{-0.4}	10.78 ± 0.20	0.18 ± 0.07	350 ± 160
A2GS35 ^(†)	4.73	10.94	12.77 ± 0.02	1001 ± 41	2.65 ± 0.11	3.48 ± 0.02	(...)	10.48 ± 0.20	0.26 ± 0.09	30 ± 14
A2GS36 ^(†)	2.36	11.27	12.06 ± 0.02	196 ± 10	0.69 ± 0.03	8.52 ± 0.02	34.5 ^{+3.3} _{-1.0}	10.54 ± 0.20	0.16 ± 0.06	175 ± 81
A2GS37 ^(*)	3.85	11.16	12.33 ± 0.07	372 ± 63	0.76 ± 0.13	8.54 ± 0.07	(...)	10.67 ± 0.21	0.25 ± 0.09	126 ± 65
A2GS38 ^(*)	(...)	(...)	(...)	(...)	(...)	(...)	(...)	(...)	(...)	(...)
A2GS39	2.36	10.61	12.44 ± 0.01	478 ± 7	6.02 ± 0.09	8.77 ± 0.01	40.9 ^{+0.4} _{-0.4}	10.96 ± 0.20	0.69 ± 0.10	192 ± 88
A2GS40 ^(*)	2.46	10.21	12.40 ± 0.09	432 ± 86	13.1 ± 2.6	8.57 ± 0.09	(...)	10.92 ± 0.22	0.84 ± 0.07	192 ± 100
A2GS41	1.759	10.54	11.88 ± 0.01	129 ± 4	2.58 ± 0.08	9.06 ± 0.01	28.3 ^{+1.0} _{-0.8}	11.20 ± 0.20	0.82 ± 0.07	1220 ± 560
A2GS42 ^(†)	2.29	11.12	12.13 ± 0.02	233 ± 9	1.09 ± 0.04	8.80 ± 0.02	34.9 ^{+2.2} _{-1.0}	10.84 ± 0.20	0.35 ± 0.10	300 ± 140
A2GS43	3.54	10.54	12.88 ± 0.02	1319 ± 52	12.45 ± 0.49	8.53 ± 0.02	65.8 ^{+3.0} _{-1.4}	10.85 ± 0.20	0.67 ± 0.10	54 ± 25
A2GS44 ^(†)	4.19	11.05	12.71 ± 0.02	888 ± 34	2.12 ± 0.08	8.56 ± 0.02	(...)	10.74 ± 0.20	0.33 ± 0.10	62 ± 28

Notes. A2GS1 to A2GS44 correspond to the 100% pure source catalog in Gómez-Guijarro et al. (2022). (1) ALMA source ID with galaxies without a *Herschel* counterpart followed by (*); (2) redshift with spectroscopic redshifts shown with three decimal digits (see Gómez-Guijarro et al. 2022 for the spectroscopic redshift references therein); (3) stellar mass; (4) IR luminosity (8–1000 μm rest-frame) as obtained from *Stardust* for the galaxies with a *Herschel* counterpart accounting for star formation only (without AGN contribution) or from the iterative approach using the dust SED libraries by Schreiber et al. (2018) for the galaxies without a *Herschel* counterpart (see Sect. 3.2); (5) total SFR accounting for the contribution of the obscured star formation probed in the IR (SFR_{IR}) and the unobscured star formation probed in the UV (SFR_{UV}); (6) distance to the MS (where the MS is from Schreiber et al. 2015) defined as the ratio of the SFR to the SFR of the MS at the same stellar mass and redshift ($\Delta\text{MS} = \text{SFR}/\text{SFR}_{\text{MS}}$); (7) dust mass as obtained from *Stardust* for the galaxies with a *Herschel* counterpart or from the iterative approach using the dust SED libraries by Schreiber et al. (2018) for the galaxies without a *Herschel* counterpart (see Sect. 3.2); (8) dust temperature obtained from a MBB fit for the galaxies with a *Herschel* counterpart (see Sect. 3.5); (9) gas mass as obtained from the metallicity-dependent gas-to-dust mass ratio technique (see Sect. 3.4); (10) gas fraction ($f_{\text{gas}} = M_{\text{gas}}/(M_{\text{gas}} + M_*)$); (11) depletion timescale ($\tau_{\text{dep}} = M_{\text{gas}}/\text{SFR}$) (see Sect. 3.4). A2GS33 and A2GS38 lack any estimate as these are K_s dropouts (A2GS33 a candidate *Spitzer*/IRAC 3.6 μm dropout) and, thus, they lack of robust redshift and stellar mass estimates to attempt an IR SED fitting and to derive dust and stellar-based properties (see Gómez-Guijarro et al. 2022). We note that among the galaxies with a *Herschel* counterpart there are two galaxies for which the mid-IR to mm photometry is not satisfactory and we treated them following the iterative approach with the dust SED libraries by Schreiber et al. (2018) (namely A2GS7 and A2GS12). Besides, some of the galaxies lack a T_{dust} estimate as they did not meet the MBB fitting criteria or the mid-IR to millimeter photometry was scarce and the fit did not converge (see Sect. 3.5). Galaxies classified as SBs in the MS following the definition in Sect. 4 are highlighted with (†).

3.2. Infrared SED fitting

SEDs in the mid-IR to mm for the galaxy sample can be divided in two groups depending on whether they have a *Herschel* counterpart or not. Therefore, we performed two types of SED fitting to the mid-IR to mm photometry.

For the galaxies with a *Herschel* counterpart (69/88) we employed the panchromatic SED fitting tool *Stardust*² developed by Kokorev et al. (2021). In summary, this code performs a multi-component fit that combines linearly stellar libraries, AGN torus templates, and IR models of dust emission

² <https://github.com/VasilyKokorev/stardust>

Table 2. Dust and stellar-based properties.

ID	z	$\log(M_*/M_\odot)$	$\log(L_{\text{IR}}/L_\odot)$	SFR ($M_\odot \text{ yr}^{-1}$)	ΔMS	$\log(M_{\text{dust}}/M_\odot)$	T_{dust} (K)	$\log(M_{\text{gas}}/M_\odot)$	f_{gas}	τ_{dep} (Myr)
(1)	(2)	(3)	(4)	(5)	(6)	(7)	(8)	(9)	(10)	(11)
A2GS45 ^(†)	2.77	11.06	11.99 ± 0.03	168 ± 13	0.66 ± 0.05	8.50 ± 0.03	37.8 ^{+2.8} _{-4.8}	10.59 ± 0.20	0.26 ± 0.09	230 ± 110
A2GS46	1.910	10.96	12.59 ± 0.01	673 ± 5	5.37 ± 0.04	8.64 ± 0.01	41.6 ^{+0.4} _{-0.5}	10.68 ± 0.20	0.35 ± 0.10	72 ± 33
A2GS47 ^(*)	3.83	10.03	12.30 ± 0.13	340 ± 100	9.51 ± 2.86	8.16 ± 0.13	(...)	10.73 ± 0.24	0.83 ± 0.08	156 ± 97
A2GS48	2.926	10.07	12.09 ± 0.03	211 ± 14	7.29 ± 0.48	8.54 ± 0.03	(...)	11.00 ± 0.20	0.90 ± 0.04	470 ± 220
A2GS49	1.973	10.31	11.83 ± 0.02	116 ± 6	3.50 ± 0.19	8.63 ± 0.02	34.8 ^{+5.0} _{-2.3}	10.87 ± 0.20	0.78 ± 0.08	580 ± 270
A2GS50	2.89	10.31	11.97 ± 0.04	159 ± 13	3.21 ± 0.27	8.55 ± 0.04	(...)	10.91 ± 0.20	0.80 ± 0.07	500 ± 240
A2GS51	2.36	10.83	11.81 ± 0.04	110 ± 11	0.85 ± 0.09	8.83 ± 0.04	(...)	10.96 ± 0.20	0.57 ± 0.11	790 ± 380
A2GS52	0.88	9.54	10.83 ± 0.06	12 ± 2	4.14 ± 0.60	9.08 ± 0.06	20.4 ^{+3.7} _{-2.0}	11.38 ± 0.21	0.99 ± 0.01	20000 ± 10000
A2GS53	2.024	10.53	11.39 ± 0.06	43 ± 6	0.75 ± 0.11	9.12 ± 0.06	(...)	11.29 ± 0.21	0.85 ± 0.06	4400 ± 2200
A2GS54	0.735	10.06	11.30 ± 0.01	34 ± 1	4.14 ± 0.10	8.94 ± 0.01	23.2 ^{+0.4} _{-0.3}	11.03 ± 0.20	0.90 ± 0.04	3100 ± 1400
A2GS55	1.545	10.76	11.84 ± 0.01	118 ± 3	1.77 ± 0.04	8.73 ± 0.01	32.4 ^{+0.5} _{-0.6}	10.79 ± 0.20	0.51 ± 0.11	520 ± 240
A2GS56 ^(†)	2.78	11.04	12.40 ± 0.02	437 ± 22	1.78 ± 0.09	8.45 ± 0.02	48.0 ^{+3.6} _{-1.3}	10.55 ± 0.20	0.24 ± 0.08	81 ± 38
A2GS57 ^(†)	4.64	11.15	12.86 ± 0.01	1233 ± 38	2.06 ± 0.06	8.50 ± 0.01	54.6 ^{+1.1} _{-1.0}	10.67 ± 0.20	0.25 ± 0.09	38 ± 17
A2GS58 ^(†)	1.83	11.03	12.14 ± 0.01	239 ± 8	1.81 ± 0.06	8.57 ± 0.01	38.3 ^{+1.4} _{-0.6}	10.59 ± 0.20	0.27 ± 0.09	161 ± 74
A2GS59 ^(†)	2.475	11.40	12.06 ± 0.03	199 ± 12	0.54 ± 0.03	8.20 ± 0.03	48.3 ^{+5.3} _{-2.5}	10.19 ± 0.20	0.06 ± 0.03	78 ± 36
A2GS60	1.120	10.53	11.30 ± 0.01	34 ± 1	1.13 ± 0.01	8.33 ± 0.01	28.0 ^{+0.2} _{-0.3}	10.38 ± 0.20	0.41 ± 0.11	700 ± 320
A2GS61	1.615	11.40	12.16 ± 0.01	249 ± 5	1.47 ± 0.03	9.17 ± 0.01	31.1 ^{+0.8} _{-0.6}	11.11 ± 0.20	0.34 ± 0.10	510 ± 230
A2GS62	1.120	10.82	11.76 ± 0.01	99 ± 1	2.04 ± 0.02	8.79 ± 0.01	28.1 ^{+0.3} _{-0.2}	10.78 ± 0.20	0.47 ± 0.11	600 ± 280
A2GS63	3.19	10.54	12.37 ± 0.01	400 ± 13	4.26 ± 0.14	8.22 ± 0.01	52.9 ^{+1.1} _{-1.6}	10.52 ± 0.20	0.49 ± 0.11	82 ± 38
A2GS64	2.67	10.67	12.07 ± 0.06	204 ± 27	1.96 ± 0.26	8.51 ± 0.06	(...)	10.71 ± 0.21	0.52 ± 0.12	250 ± 120
A2GS65 ^(†)	2.22	11.15	12.36 ± 0.01	395 ± 10	1.85 ± 0.05	8.86 ± 0.01	40.2 ^{+1.0} _{-0.4}	10.89 ± 0.20	0.35 ± 0.10	194 ± 89
A2GS66 ^(†)	1.686	10.81	12.03 ± 0.01	185 ± 3	2.28 ± 0.04	8.31 ± 0.01	37.2 ^{+0.6} _{-1.2}	10.37 ± 0.20	0.27 ± 0.09	127 ± 58
A2GS67 ^(*)	0.650	10.30	11.92 ± 0.08	142 ± 26	11.81 ± 2.20	8.63 ± 0.08	(...)	10.65 ± 0.21	0.69 ± 0.11	310 ± 170
A2GS68	1.413	10.10	11.60 ± 0.01	69 ± 2	4.63 ± 0.13	8.37 ± 0.01	35.2 ^{+1.0} _{-0.8}	10.59 ± 0.20	0.76 ± 0.08	540 ± 250
A2GS69	1.414	10.89	11.93 ± 0.01	147 ± 2	2.00 ± 0.03	8.82 ± 0.01	31.4 ^{+0.3} _{-0.4}	10.83 ± 0.20	0.46 ± 0.11	460 ± 210
A2GS70 ^(*)	2.61	9.61	12.28 ± 0.11	331 ± 81	37.46 ± 9.20	8.41 ± 0.11	(...)	11.05 ± 0.23	0.97 ± 0.02	340 ± 200
A2GS71 ^(*)	3.026	10.26	12.48 ± 0.07	553 ± 82	11.90 ± 1.76	8.52 ± 0.07	(...)	10.91 ± 0.21	0.82 ± 0.07	150 ± 75
A2GS72 ^(*)	2.28	9.37	11.99 ± 0.21	171 ± 80	38.85 ± 18.30	8.20 ± 0.21	(...)	10.91 ± 0.29	0.97 ± 0.02	480 ± 390
A2GS73	1.987	10.15	12.25 ± 0.01	309 ± 5	13.40 ± 0.22	8.46 ± 0.01	42.1 ^{+0.6} _{-0.7}	10.77 ± 0.20	0.81 ± 0.07	185 ± 84
A2GS74	1.61	11.31	11.71 ± 0.02	89 ± 4	0.58 ± 0.02	8.89 ± 0.02	29.3 ^{+2.3} _{-0.7}	10.84 ± 0.20	0.25 ± 0.09	780 ± 360
A2GS75 ^(†)	1.618	11.25	12.35 ± 0.01	386 ± 4	2.65 ± 0.02	8.91 ± 0.01	36.9 ^{+0.3} _{-0.5}	10.87 ± 0.20	0.30 ± 0.10	194 ± 88
A2GS76	2.53	11.24	11.76 ± 0.05	98 ± 12	0.32 ± 0.04	8.52 ± 0.05	34.5 ^{+4.0} _{-3.0}	10.55 ± 0.21	0.17 ± 0.07	360 ± 170
A2GS77 ^(†)	2.805	10.55	12.02 ± 0.03	179 ± 13	2.14 ± 0.15	7.98 ± 0.03	56.0 ^{+7.4} _{-4.1}	10.23 ± 0.20	0.32 ± 0.10	91 ± 43
A2GS78 ^(*)	3.65	10.15	12.28 ± 0.13	335 ± 96	7.48 ± 2.15	8.17 ± 0.13	(...)	10.67 ± 0.24	0.77 ± 0.10	141 ± 87
A2GS79	1.998	10.94	12.42 ± 0.01	454 ± 5	3.52 ± 0.04	8.54 ± 0.01	43.7 ^{+0.3} _{-0.5}	10.60 ± 0.20	0.32 ± 0.10	87 ± 40
A2GS80 ^(†)	1.314	11.06	11.55 ± 0.01	61 ± 2	0.74 ± 0.02	8.29 ± 0.01	36.0 ^{+2.0} _{-1.6}	10.25 ± 0.20	0.13 ± 0.05	290 ± 130
A2GS81	2.66	10.63	11.75 ± 0.05	97 ± 11	1.02 ± 0.11	8.57 ± 0.05	(...)	10.79 ± 0.20	0.59 ± 0.11	630 ± 300
A2GS82 ^(*)	4.38	10.61	12.15 ± 0.13	242 ± 74	1.51 ± 0.46	8.22 ± 0.13	(...)	10.57 ± 0.24	0.48 ± 0.14	153 ± 97
A2GS83 ^(†)	2.130	11.00	12.08 ± 0.01	207 ± 5	1.32 ± 0.03	8.37 ± 0.01	42.1 ^{+0.7} _{-0.9}	10.43 ± 0.20	0.21 ± 0.08	123 ± 56
A2GS84	4.36	10.74	12.89 ± 0.03	1322 ± 76	6.13 ± 0.35	8.35 ± 0.03	66.8 ^{+1.7} _{-1.0}	10.66 ± 0.20	0.45 ± 0.11	34 ± 16
A2GS85	2.72	10.77	12.07 ± 0.03	201 ± 12	1.51 ± 0.09	8.71 ± 0.03	38.7 ^{+1.4} _{-1.9}	10.88 ± 0.20	0.56 ± 0.11	380 ± 170
A2GS86 ^(*)	1.95	10.12	12.16 ± 0.12	251 ± 71	11.91 ± 3.38	8.45 ± 0.12	(...)	10.76 ± 0.23	0.81 ± 0.08	230 ± 140
A2GS87 ^(*)	3.32	10.56	12.08 ± 0.13	207 ± 60	2.01 ± 0.59	8.41 ± 0.13	(...)	10.71 ± 0.24	0.59 ± 0.13	250 ± 150
A2GS88	0.123	10.21	10.35 ± 0.01	4 ± 1	0.90 ± 0.01	8.13 ± 0.01	22.8 ^{+0.1} _{-0.1}	10.05 ± 0.20	0.41 ± 0.11	2900 ± 1300

Notes. A2GS45 to A2GS88 correspond to the prior-based source catalog in Gómez-Guijarro et al. (2022).

from star formation. All three components are fit simultaneously yet independently from each other, without assuming an energy balance between UV emission absorbed and re-emitted by dust at far-IR and mm wavelengths. An energy-balanced solution implies cospatial stellar and dust continuum emission (e.g., da Cunha et al. 2008), an assumption that is applicable and physically motivated in a wide variety of SFGs, but perhaps not valid for all dusty SFGs (DSFGs). Stars and dust are not always physically connected, with samples of DSFGs exhibiting differences in their stellar and dust continuum distributions sometimes spatially offset from each other (e.g., Simpson et al. 2015; Hodge et al. 2016; Gómez-Guijarro et al. 2018; Elbaz et al. 2018; Franco et al. 2018). The code finds the best linear combination of a set of basic templates (similar to eigenvectors in principal component analysis), instead of using a vast library of templates. The models used to create the basic templates are: (1) a stellar library (12 templates)

composed of an updated version of the single stellar population synthesis models in Brammer et al. (2008). The stellar component helps to constrain the AGN contribution in the near/mid-IR; (2) an AGN library consisting in empirically-derived templates from Mullaney et al. (2011) that describe the AGN emission from 6 to 100 μm rest-frame, using both high and low-luminosity AGN templates; (3) an IR library composed of 4862 Draine & Li (2007) dust emission templates with the correction from Draine et al. (2014). These models combine two components: a cold dust component coming from the diffuse interstellar medium (ISM) heated by a minimum radiation field, U_{min} , and a warm dust component associated with photodissociation regions (PDRs) heated by a power law distribution of starlight with intensities ranging from U_{min} to U_{max} . The relative contribution between the two components is quantified by the parameter γ , giving the fraction of dust mass associated with the warm dust component in PDRs. The properties of the dust grains in

the models are parametrized by the polycyclic aromatic hydrocarbon (PAH) index q_{PAH} , yielding the fraction of dust mass in the form of PAH grains; (4) radio continuum data are not fit by the code. The radio model is a power law $S_\nu \propto \nu^\alpha$ with a fixed spectral index of $\alpha = -0.75$. The output radio luminosity at 1.4 GHz rest-frame is such that satisfies the IR-radio correlation by [Delvecchio et al. \(2021\)](#), which depends on the stellar mass of a given galaxy.

As described by [Draine & Li \(2007\)](#), the infinitesimal portion of the dust mass dM_{dust} exposed to a radiation field with intensities between U and $U + dU$ can be expressed as a combination of a δ -function, accounting for the cold dust component heated by U_{min} , and a power law distribution of starlight from U_{min} to U_{max} :

$$\frac{dM_{\text{dust}}}{dU} = (1 - \gamma)M_{\text{dust}}\delta(U - U_{\text{min}}) + \gamma M_{\text{dust}} \frac{\alpha - 1}{U_{\text{min}}^{1-\alpha} - U_{\text{max}}^{1-\alpha}} U^{-\alpha} \quad (1)$$

with $U_{\text{min}} \leq U_{\text{max}}$ and $\alpha \neq 1$. The values (q_{PAH} , U_{min} , γ) are obtained from the result of the fit, considering a fixed $U_{\text{max}} = 10^6$ and $\alpha = 2$ following [Draine et al. \(2007\)](#). The total dust mass (M_{dust}) is then calculated from the normalization and the total IR luminosity by integrating the fit in the range 8–1000 μm rest-frame. Considering the fraction of the total IR luminosity that is due to AGN contribution (f_{AGN}) from the fitting procedure, it is ensured that the IR luminosity (L_{IR}) used hereafter accounts for star formation only:

$$L_{\text{IR}} = (1 - f_{\text{AGN}}) \int_{8\mu\text{m}}^{1000\mu\text{m}} L_\nu(\lambda) \times \frac{c}{\lambda^2} d\lambda. \quad (2)$$

For galaxies without a *Herschel* counterpart (19/88), we employed an iterative approach using the IR template library of [Schreiber et al. \(2018\)](#). This library considers an evolution of the dust temperature (T_{dust}) with redshift and distance to the MS (ΔMS), defined as the ratio of the SFR to the SFR of the MS at the same stellar mass and redshift ($\Delta\text{MS} = \text{SFR}/\text{SFR}_{\text{MS}}$), as well as the dependency of the mid-to-total infrared color ($\text{IR8} = L_{\text{IR}}/L_8$) with ΔMS . Therefore, it is possible to define MS ($\Delta\text{MS} = 1$) and SB ($\Delta\text{MS} = 5$) templates. The templates are normalized to $M_{\text{dust}} = 1 M_\odot$. The total M_{dust} is then calculated by re-normalizing to the 1.1 mm flux density and the total L_{IR} by integrating the SED in the range 8–1000 μm rest-frame.

For each galaxy, the output L_{IR} along with the galaxy redshift and stellar mass (see Sect. 3.1) was used to calculate its ΔMS . If the resulting ΔMS after normalizing the MS template was within the 1σ scatter of the MS, which corresponds to $\Delta\text{MS} < 2$ (~ 0.3 dex; e.g., [Noeske et al. 2007](#); [Whitaker et al. 2012](#); [Schreiber et al. 2015](#)) and, simultaneously, ΔMS after normalizing the SB template went in the direction of the MS reaching at least within the 2σ scatter of the MS ($\Delta\text{MS} < 4$), then a MS template was considered as the appropriate one. The opposite was true, if the resulting ΔMS after normalizing with the SB template was outside the 2σ scatter of the MS ($\Delta\text{MS} > 4$) and, simultaneously, ΔMS after normalizing with the MS template went in the direction of the SBs reaching further than the 2σ scatter of the MS, then a SB template was considered as the appropriate one. For all the galaxies without a *Herschel* counterpart in our sample, the above conditions were satisfied and we chose either a MS or a SB template for each galaxy. Although not relevant for the analysis in this work, it is interesting to note that the latter was even true for the galaxies with a *Herschel* counterpart, except just in two cases (namely A2GS53 and A2GS62) where $\Delta\text{MS} < 2$ with the MS template, but $\Delta\text{MS} > 4$ with the SB template. From the estimates as obtained by *Stardust* (the

two have a *Herschel* counterpart) both are in the MS within a factor 3 ($0.33 < \Delta\text{MS} < 3$, 0.5 dex).

When comparing M_{dust} estimates it is important to take into account possible physical differences in the dust models. As explained by [Schreiber et al. \(2018\)](#) the dust models in their IR template library assume dust grain species with different emissivities that lead to systematically lower M_{dust} values compared to those from [Draine & Li \(2007\)](#) dust models. Therefore, in order for the M_{dust} estimates to be comparable in galaxies with and without a *Herschel* counterpart, we scaled the M_{dust} estimates obtained using the dust SED libraries by [Schreiber et al. \(2018\)](#) to account for the physical difference in the dust models following [Schreiber et al. \(2018\)](#).

As a sanity test, we compared M_{dust} and L_{IR} estimates for the galaxies with a *Herschel* counterpart as obtained by both *Stardust* and the iterative approach using the dust SED libraries by [Schreiber et al. \(2018\)](#). The results are consistent on average with a relatively large dispersion with a median relative difference $(M_{\text{dust}}^{\text{Sch18}} - M_{\text{dust}}^{\text{Stardust}})/M_{\text{dust}}^{\text{Stardust}} = -0.01 \pm 0.45$ and $(L_{\text{IR}}^{\text{Sch18}} - L_{\text{IR}}^{\text{Stardust}})/L_{\text{IR}}^{\text{Stardust}} = -0.07 \pm 0.71$ (where the uncertainty is the median absolute deviation). A large dispersion was expected since for the iterative approach using the dust SED libraries by [Schreiber et al. \(2018\)](#) only the 1.1 mm flux densities were considered.

In Tables 1 and 2 we present M_{dust} and L_{IR} estimates as obtained by *Stardust* for the galaxies with a *Herschel* counterpart and the iterative approach using the dust SED libraries by [Schreiber et al. \(2018\)](#) for the galaxies without a *Herschel* counterpart. The uncertainties were calculated performing 10 000 Monte-Carlo simulations perturbing the photometry randomly within the uncertainties. Appendix A collects the different SED fits to the mid-IR to mm photometry for the galaxy sample. Inspecting the results, there are two galaxies with *Herschel* counterparts for which the mid-IR to mm photometry is not satisfactory as it is still affected by blending (namely A2GS7 and A2GS12). The de-blending methodology for SPIRE was optimized for the entire *Herschel* mosaic. Therefore, there could still exist some specific single source cases reflecting some level of contamination by blending (as it is the case for A2GS7 and A2GS12). We treated them as if they were galaxies without a *Herschel* counterpart instead, with their M_{dust} and L_{IR} obtained following the iterative approach with the dust SED libraries by [Schreiber et al. \(2018\)](#). Note also that, having reassessed the *Herschel* counterpart assignment in this work for the sources in common with [Franco et al. \(2020a\)](#), it resulted in some additional galaxies to have *Herschel* detections respect to [Franco et al. \(2020a\)](#).

3.3. Star formation rates

The total SFR accounts for the contribution of the obscured star formation probed in the IR (SFR_{IR}) and the unobscured star formation probed in the UV (SFR_{UV}):

$$\text{SFR} = \text{SFR}_{\text{IR}} + \text{SFR}_{\text{UV}}. \quad (3)$$

We calculated the obscured star formation through L_{IR} as derived in Sect. 3.2 using the [Kennicutt \(1998\)](#) conversion (we note that we considered the fraction of the total IR luminosity that is due to AGN contribution and L_{IR} accounts for star formation only):

$$\text{SFR}_{\text{IR}}(M_\odot \text{ yr}^{-1}) = 1.72 \times 10^{-10} L_{\text{IR}}(L_\odot). \quad (4)$$

The unobscured star formation can be obtained through the UV luminosity (L_{UV}) using the conversion from

Daddi et al. (2004):

$$\text{SFR}_{\text{UV}}(M_{\odot} \text{ yr}^{-1}) = 2.16 \times 10^{-10} L_{\text{UV}}(L_{\odot}), \quad (5)$$

where L_{UV} is given by the rest-frame 1500 Å luminosity:

$$L_{\text{UV}}(L_{\odot}) = 4\pi d_L^2 \frac{\nu_{1500}}{(1+z)} \frac{10^{-0.4(48.6+m_{1500})}}{3.826 \times 10^{33}}, \quad (6)$$

with d_L the luminosity distance (cm), ν_{1500} the frequency (Hz) that corresponds to $\lambda = 1500$ Å, and m_{1500} the rest-frame 1500 Å (AB) magnitude that we obtained from the ZFOURGE catalog for the stellar counterpart of each ALMA source. For the galaxies which we updated the default ZFOURGE redshifts and photometry for as explained in Sect. 3.1, we derived rest-frame 1500 Å magnitudes employing the same methodology as ZFOURGE: a top hat filter centered at 1500 Å with a 350 Å width.

In comparison with the estimates in Franco et al. (2020a) for the sources in common with this work, SFR estimates are consistent on average with a small dispersion of 20%.

3.4. Gas masses

The gas mass reservoir (M_{gas}) in galaxies can be determined through the dust emission. We employed the gas-to-dust mass ratio (δ_{GDR}) with a metallicity dependency (e.g., Magdis et al. 2011, 2012; Berta et al. 2016):

$$M_{\text{gas}} = \delta_{\text{GDR}}(Z) M_{\text{dust}}. \quad (7)$$

This technique converts M_{dust} to M_{gas} through a well-established relation between δ_{GDR} and the gas-phase metallicity of galaxies ($\delta_{\text{GDR}}-Z$), seen both in the local universe and at high redshift (e.g., Leroy et al. 2011; Magdis et al. 2012; Rémy-Ruyer et al. 2014; Genzel et al. 2015; Coogan et al. 2019). Here we used the $\delta_{\text{GDR}}-Z$ relation of Magdis et al. (2012):

$$\log \delta_{\text{GDR}} = (10.54 \pm 1.00) - (0.99 \pm 0.12)(12 + \log(\text{O}/\text{H})). \quad (8)$$

Direct metallicity measurements are unknown for our galaxy sample and, in general, elusive for DSFGs. We employed a mass–metallicity relation (MZR; e.g., Erb et al. 2006) to calculate the metallicities for the galaxy sample. In particular, we used the redshift-dependent MZR expression of Genzel et al. (2015):

$$12 + \log(\text{O}/\text{H}) = a - 0.087(\log(M_*/1.7) - b)^2, \quad (9)$$

where $a = 8.74$ and $b = 10.4 + 4.46 \log(1+z) - 1.78 \log(1+z)^2$. We included a 1.7 factor to convert our stellar masses and SFRs from a Salpeter (Salpeter 1955) to a Chabrier (Chabrier 2003) IMF (e.g., Reddy et al. 2006; Santini et al. 2012; Elbaz et al. 2018), as the latter is the IMF used in the MZR by Genzel et al. (2015). The resulting metallicities are calibrated in the Pettini & Pagel (2004, PP04 N2) scale, the calibration used in Eq. (8) by Magdis et al. (2012). We adopted an uncertainty of 0.2 dex in the metallicities (Magdis et al. 2012).

Having calculated the gas-phase metallicities, we used Eq. (8) to derive δ_{GDR} for each galaxy and converted M_{dust} into M_{gas} using Eq. (7). We note that these M_{gas} estimates yield the total gas budget of the galaxies, including the molecular (M_{H_2}) and the atomic phase (M_{HI}): $M_{\text{gas}} = M_{\text{H}_2} + M_{\text{HI}}$. A variety of studies have suggested that for the redshifts and relatively massive galaxies probed in our work, the molecular gas dominates over the atomic gas within the physical scales probed by the dust continuum observations at 1.1 mm (e.g.,

Obreschkow & Rawlings 2009; Tacconi et al. 2010; Daddi et al. 2010).

In Tables 1 and 2 we present M_{gas} estimates for the galaxies in our sample along with gas fractions ($f_{\text{gas}} = M_{\text{gas}}/(M_{\text{gas}} + M_*)$) and depletion timescales ($\tau_{\text{dep}} = M_{\text{gas}}/\text{SFR}$), the latter being by definition the inverse of the star formation efficiency (SFE = $1/\tau_{\text{dep}}$).

However, another description of metallicities is the so-called fundamental metallicity relation (FMR; Mannucci et al. 2010). The FMR incorporates an additional dependency of metallicity on the SFR. We obtained alternative M_{gas} estimates using the FMR expression of Mannucci et al. (2010):

$$12 + \log(\text{O}/\text{H}) = 8.90 + 0.37m - 0.14s - 0.19m^2 + 0.12ms - 0.054s^2, \quad (10)$$

where $m = \log(M_*/1.7) - 10$ and $s = \log \text{SFR}/1.7$ (solar units). Once again, a 1.7 factor is included to convert our stellar masses and SFRs from a Salpeter (Salpeter 1955) to a Chabrier (Chabrier 2003) IMF, as the latter is the IMF used in the FMR by Mannucci et al. (2010). The resulting metallicities are calibrated for the Kewley & Dopita (2002, KD02) photoionization models. We converted them to the PP04 N2 scale, the calibration used in Eq. (8) by Magdis et al. (2012), following the conversion recipes by Kewley & Ellison (2008).

The median relative difference between MZR and FMR M_{gas} estimates is $(M_{\text{gas}}^{\text{FMR}} - M_{\text{gas}}^{\text{MZR}})/M_{\text{gas}}^{\text{MZR}} = 0.37 \pm 0.22$. While the dispersion is relatively small, the MZR M_{gas} estimates are systematically lower than those from the FMR. This is expected as the FMR dependency on SFR results in galaxies with a higher SFR to have lower metallicities at a fixed stellar mass and, thus, higher δ_{GDR} and M_{gas} .

In any case, metallicities are poorly constrained in general for DSFGs, SBs and at $z > 3$ (e.g., Tan et al. 2013; Kewley et al. 2013; Steidel et al. 2014). The extent to which the MZR or FMR are preferable for DSFGs is an open question and beyond the scope of this paper. In this work the estimates reported and used hereafter are those from MZR. We opted for this choice as the scaling relations for τ_{dep} and f_{gas} from Tacconi et al. (2018) employed in the following Sects. 4 and 5 used the MZR and, particularly, that of Genzel et al. (2015), allowing for a direct comparison. The MZR in Genzel et al. (2015) accounts for a redshift evolution and it is applied in Tacconi et al. (2018) for galaxies at $0 < z < 4$ and stellar masses ranging $\log(M_*/M_{\odot}) = 9.0-11.8$, which span almost the totality of our galaxy sample. In addition, MZR was also the choice for the follow up on the GOODS-ALMA 1.0 galaxy sample presented in Franco et al. (2020a), permitting a consistent analysis and direct comparison. Regardless, the results presented in the following Sects. 4 and 5 using the MZR are reproduced for the FMR and a fixed solar metallicity in Appendix C.

Another possibility to derive M_{gas} via the dust emission is by employing a single-band measurement of the dust continuum flux in the Rayleigh-Jeans (RJ) side of the IR SED (e.g., Scoville et al. 2014; Groves et al. 2015; Schinnerer et al. 2016). For this technique we followed Scoville et al. (2016), resulting in M_{gas} estimates consistent on average within 25% and a relatively large dispersion compared to those obtained from the $\delta_{\text{GDR}}-Z$ technique, both with the MZR and the FMR. The median relative differences are $(M_{\text{gas}}^{\text{RJ}} - M_{\text{gas}}^{\text{GDR}-Z(\text{MZR})})/M_{\text{gas}}^{\text{GDR}-Z(\text{MZR})} = 0.23 \pm 0.84$ and $(M_{\text{gas}}^{\text{RJ}} - M_{\text{gas}}^{\text{GDR}-Z(\text{FMR})})/M_{\text{gas}}^{\text{GDR}-Z(\text{FMR})} = -0.15 \pm 0.87$. We note that the RJ technique also accounts for the total gas budget of the galaxies, including M_{H_2} and M_{HI} . While the RJ technique is a very powerful tool to derive M_{gas} estimates for large

galaxy samples at a relatively cheap observational cost, it has limitations as it does not take into account the evolution of the gas-phase metallicity or the mass-weighted T_{dust} of galaxies with redshift at a fixed stellar mass (e.g., Genzel et al. 2015; Berta et al. 2016; Schinnerer et al. 2016; Magdis et al. 2017; Harrington et al. 2021). Therefore, we adopted M_{gas} estimates from the $\delta_{\text{GDR}}-Z$ technique instead.

In comparison with the estimates in Franco et al. (2020a) for the sources in common with this work, M_{gas} estimates are on average 10% systematically higher with a relatively small dispersion of 30%. This systematic difference is in perfect agreement with the systematically 10% higher 1.1 mm flux densities reported in Gómez-Guijarro et al. (2022) compared to those in Franco et al. (2018, 2020b).

3.5. Dust temperatures

Complementary to the IR SED fits in Sect. 3.2, we also fit the mid-IR to mm photometry of the galaxies with a *Herschel* counterpart employing a single-temperature optically-thin modified blackbody (MBB) with the purpose of deriving luminosity-weighted T_{dust} estimates (e.g., Hwang et al. 2010; Magdis et al. 2011, 2012; Magnelli et al. 2012, 2014). The MBB is given by:

$$S_{\nu} \propto \frac{\nu^{3+\beta}}{e^{\frac{h\nu}{kT_{\text{dust}}}} - 1} \quad (11)$$

where T_{dust} is the effective dust temperature and β is the effective dust emissivity index.

Following the criteria of Hwang et al. (2010), also applied by Franco et al. (2020a): (1) we considered observed datapoints at $\lambda_{\text{rf}} \geq 0.55 \lambda_{\text{peak}}$ to avoid emission from small grains that dominate the dust emission at shorter wavelengths, with λ_{peak} given by the Stardust fit; (2) we required at least one datapoint at $0.55 \lambda_{\text{peak}} \leq \lambda_{\text{rf}} \leq \lambda_{\text{peak}}$ (met by all galaxies except two, namely A2GS20 and A2GS53); and (3) we required at least one datapoint at $\lambda_{\text{rf}} \geq \lambda_{\text{peak}}$ (excluding the radio data dominated by synchrotron emission). We assumed a fixed value of $\beta = 1.5$ typical for DSFGs (e.g., Hildebrand 1983; Kovács et al. 2006; Gordon et al. 2010).

In Tables 1 and 2 we present T_{dust} estimates for the galaxies with a *Herschel* counterpart and the result of the MBB fit is depicted in Appendix A. The uncertainties were calculated performing 10 000 Monte-Carlo simulations perturbing the photometry randomly within the uncertainties. There are some galaxies lacking a T_{dust} estimate, in summary: (1) galaxies without a *Herschel* counterpart for which there was not enough information to attempt a T_{dust} estimation (A2GS8, A2GS10, A2GS17, A2GS18, A2GS27, A2GS29, A2GS33, A2GS37, A2GS38, and A2GS40); (2) galaxies with a *Herschel* counterpart for which the mid-IR to mm photometry was not satisfactory (A2GS7 and A2GS12); (3) galaxies that did not meet the MBB fitting criteria indicated above (A2GS20 and A2GS53); (4) galaxies for which the MBB fit did not converge (A2GS25, A2GS26, A2GS35, A2GS44, A2GS48, A2GS50, A2GS51, A2GS64, and A2GS81), typically galaxies with only SPIRE 250 μm and ALMA 1.1 mm data points.

In comparison with the estimates in Franco et al. (2020a) for the sources in common with this work, T_{dust} estimates are perfectly consistent on average with a very low dispersion of 10%.

3.6. AGN

Tracking the presence of AGN within our galaxy sample is interesting to unveil potential signs of coevolution between AGN and

star formation activity, but it is also important to check potential biases in the derived dust and stellar-based properties in the galaxies identified as AGN. We identified AGN based on X-ray, IR, or radio excesses that can not be explained based solely by star formation. First, we searched for X-ray-bright AGN by cross matching our galaxy sample with the *Chandra* Deep Field-South 7 Ms source catalog (Luo et al. 2017). Galaxies identified as AGN were those with a X-ray counterpart with an intrinsic X-ray luminosity $\log(L_{\text{X,int}}/L_{\odot}) > 42.5$ (absorption-corrected soft and hard X-ray luminosity, typically applied as a threshold for X-ray bright AGN e.g., Luo et al. 2017). We note that for the galaxies for which the redshifts differ from those in the X-ray catalog, we corrected the intrinsic X-ray luminosity assuming an intrinsic X-ray photon index $\Gamma = 1.8$ (Luo et al. 2017). 24/88 galaxies were identified as AGN based on their X-ray excess. However, it is important to note that X-ray emission from massive X-ray binaries in galaxies with high SFR such as those studied in this work could be comparable to the level expected for X-ray-bright AGN (e.g., Mineo et al. 2012). Therefore, it is plausible that in some of these galaxies identified as AGN based on the classical widespread definition for X-ray excess, the latter could be explained based solely by star formation or at least a significant fraction of it. Second, we also checked for IR-bright AGN defined as those galaxies showing a significant AGN contribution to the total IR luminosity $f_{\text{AGN}} > 20\%$ (as derived from the IR SED fitting in Sect. 3.2, typically applied as a threshold for IR-bright AGN, above which their effects are significant in the determination of L_{IR} and SFR e.g., Valentino et al. 2021). While there is a small level of AGN contribution to the IR SED in some galaxies (see Figs. A.1 and A.2), for none of them this level is large enough to be classified as AGN. Finally, we also checked for radio-bright AGN applying a radio-excess criterion (e.g., Donley et al. 2005; Del Moro et al. 2013; Delvecchio et al. 2017). Galaxies identified as AGN were those having a significantly low IR/radio ratio (q_{IR}) located $>3\sigma$ below the scatter of the infrared-radio correlation (IRRC; e.g., de Jong et al. 1985; Helou et al. 1985; Condon 1992), following the IRRC definition of Delvecchio et al. (2021) for a given stellar mass and redshift. While some galaxies display a small radio excess compared to the predictions of the IRRC for their stellar mass and redshift (see Figs. A.1 and A.2), for none of them this level is large enough to be classified as AGN. Although not classified as radio-bright AGN, A2GS34 exhibits an inverted radio spectra, which could be a sign of a compact radio core (e.g., Kellermann & Pauliny-Toth 1969). Nevertheless, A2GS34 was already classified as a X-ray-bright AGN. In summary, we find evidence for AGN in 27% of the galaxies in our sample.

3.7. Completeness and selection limits

The GOODS-ALMA 2.0 survey reaches a $\sim 100\%$ completeness at flux densities $S_{1.1\text{mm}} > 1 \text{ mJy}$ for sources with dust continuum sizes up to $1''$ FWHM (see Gómez-Guijarro et al. 2022). In Fig. 1 we show the M_{gas} limit as a function of redshift that corresponds to this flux density completeness threshold. This M_{gas} limit was calculated from the M_{dust} limit by using both a MS and SB template from the dust SED libraries by Schreiber et al. (2018) normalized at $S_{1.1\text{mm}} = 1 \text{ mJy}$ as a function of redshift. Then, we employed the $\delta_{\text{GDR}}-Z$ technique for the median metallicity of our galaxy sample as calculated from the MZR. Lower (higher) metallicities would lead to higher (lower) δ_{GDR} and M_{gas} (if the FMR was assumed, metallicities would be also systematically lower at a fixed stellar mass and, thus, leading to higher δ_{GDR} and M_{gas} as well).

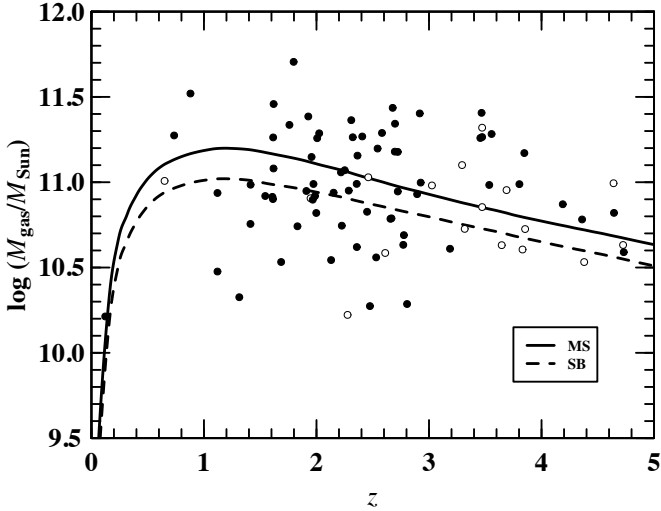


Fig. 1. M_{gas} versus redshift for our GOODS-ALMA 2.0 galaxy sample. Filled symbols represent galaxies with a *Herschel* counterpart and open symbols galaxies without a *Herschel* counterpart. The black line indicates the M_{gas} completeness limit as a function of redshift (solid and dashed for MS and SB templates, respectively). This limit correspond to the GOODS-ALMA 2.0 $\sim 100\%$ completeness, associated with flux densities $S_{1.1\text{mm}} > 1\text{ mJy}$ for sources with dust continuum sizes up to $1''$ FWHM (see Gómez-Guijarro et al. 2022) for the median metallicity of our galaxy sample.

As a sanity test, we checked whether the galaxies in our sample were expected to be detected by *Herschel* or not. In order to do this, we employed the dust SED libraries by Schreiber et al. (2018) to predict flux ratios between ALMA 1.1 mm and the six *Herschel* bands of PACS (70, 100, 160 μm) and SPIRE (250, 350, 500 μm). These flux ratio predictions were calculated for both MS ($\Delta\text{MS} = 1$) and SB ($\Delta\text{MS} = 5$) templates as a function of redshift. We show them in Fig. B.1 and they are tabulated in steps of 0.1 in redshift in Table B.1. We compared the flux predictions with the *Herschel* flux limits given by Leiton et al. (2015), where the authors reported 2.2 mJy for PACS 160 μm and 2.5 mJy for SPIRE 250 μm at 68% completeness in GOODS, and values three times above these flux limits resulted in a completeness of $\sim 90\%$. There were only four galaxies for which the SPIRE 250 μm flux predictions were above three times these flux limits and, thus, the galaxies should have been detected by *Herschel*. In these cases the PACS 160 μm flux predictions were also above three times the flux limits. However, in these four cases, the chosen template between MS and SB was always a SB template, with the fluxes being consistent with the limits for three of them if the chosen template was the MS one instead (namely A2GS10, A2GS40, and A2GS86). It is also important to consider that trends in T_{dust} with redshift and ΔMS come from statistical samples of the general population of SFGs (e.g., Magnelli et al. 2014; Béthermin et al. 2015; Schreiber et al. 2018), but there are exceptions of newly discovered galaxy populations that might not follow these general trends. Notably, there exists a population of SBs within the scatter of the MS, owing to their higher SFR surface densities compared to normal SFGs in the MS (Elbaz et al. 2018). These three galaxies could be closer to the MS, but having warmer T_{dust} than predicted by the general trends, which could be characteristic of SBs within the MS. At the moment, with only a single datapoint at 1.1 mm it is not possible to measure T_{dust} in these galaxies and confirm their nature and most appropriate template, so we

opted for maintaining the general approach and applied the SB template to them.

4. The main sequence and scaling relations framework in galaxy evolution

In this section we study the properties derived in Sect. 3 in the framework of scaling relations in galaxy evolution. We place them in relation with the MS and the scaling relations for depletion timescales, gas fractions, and dust temperatures.

In Fig. 2 we place our sample in the MS context, showing the location of the galaxies in the $\text{SFR}-M_*$ and $\Delta\text{MS}-M_*$ planes. The $\text{SFR}-M_*$ plane is the most typical representation of the correlation between SFR and stellar mass of SFGs, so-called MS of SFGs (e.g., Brinchmann et al. 2004; Daddi et al. 2007; Elbaz et al. 2007; Noeske et al. 2007; Whitaker et al. 2012). However, given the rise of the MS normalization with increasing redshift (e.g., Noeske et al. 2007; Whitaker et al. 2012; Speagle et al. 2014; Schreiber et al. 2015; Leslie et al. 2020), this type of representation is disadvantageous for galaxy samples that span a wide redshift range like ours. In order to overcome this limitation, we scaled the SFR estimates to a common redshift, corresponding to the median value of the sample ($z_{\text{med}} = 2.46$), using the MS from Schreiber et al. (2015). While the scaled SFR values do not reflect the true SFR estimates of the individual galaxies, the overall distribution of the galaxy sample in the $\text{SFR}-M_*$ plane maintains the ΔMS that each galaxy would have if plotted against the MS associated with its redshift. An alternative representation is to simply plot the $\Delta\text{MS}-M_*$ plane, where the SFR of each galaxy is normalized by the SFR of the MS at its stellar mass and redshift. This type of representation offers a more direct view of the distribution of the galaxy sample in the MS framework without the limitation of the $\text{SFR}-M_*$ plane for galaxy samples that cover a wide redshift range.

Our galaxy sample is located above and within the MS: 42% above the MS ($\Delta\text{MS} > 3$) and 58% are in the MS within a factor 3 ($0.33 < \Delta\text{MS} < 3$, 0.5 dex).

In the following, we focused on the subset of galaxies with a *Herschel* counterpart (69/88), so the properties presented in the different plots were obtained using the same methodology. This is particularly relevant in the case of τ_{dep} , for which a fixed MS or SB template from the dust SED libraries implies a constant $L_{\text{IR}}/M_{\text{dust}}$ ratio and, thus, $\tau_{\text{dep}} = M_{\text{gas}}/\text{SFR} \propto M_{\text{dust}}/L_{\text{IR}}$ is also constant. It is very important in the case of T_{dust} too, for which there was not enough information to attempt a T_{dust} estimation in galaxies without a *Herschel* counterpart. Galaxies with and without a *Herschel* counterpart have on average similar M_{gas} . Those without a *Herschel* counterpart have $\times 1.5$ higher SFR and $\times 2.4$ lower stellar masses on average. Consequently, galaxies without a *Herschel* counterpart have $\times 1.7$ lower τ_{dep} and $\times 1.7$ higher f_{gas} on average compared to those with a *Herschel* counterpart. Therefore, removing galaxies without a *Herschel* counterpart partially removes the low stellar mass end of lower τ_{dep} and higher f_{gas} galaxies.

In Fig. 3 our galaxy sample is placed in the context of the scaling relation for depletion timescales, gas fractions, and dust temperatures. We show τ_{dep} , f_{gas} , and T_{dust} as a function of stellar mass and ΔMS in comparison with the scaling relations established in the literature by Tacconi et al. (2018) for $\tau_{\text{dep}}(z, M_*, \Delta\text{MS})$ and $f_{\text{gas}}(z, M_*, \Delta\text{MS})$, and by Schreiber et al. (2018) for $T_{\text{dust}}(z, \Delta\text{MS})$. Similarly to Fig. 2, we show two types of representation in Fig. 3. In the first and third rows, the values are scaled to a common redshift and stellar mass (first row) and to a common redshift and ΔMS (third row) corresponding to

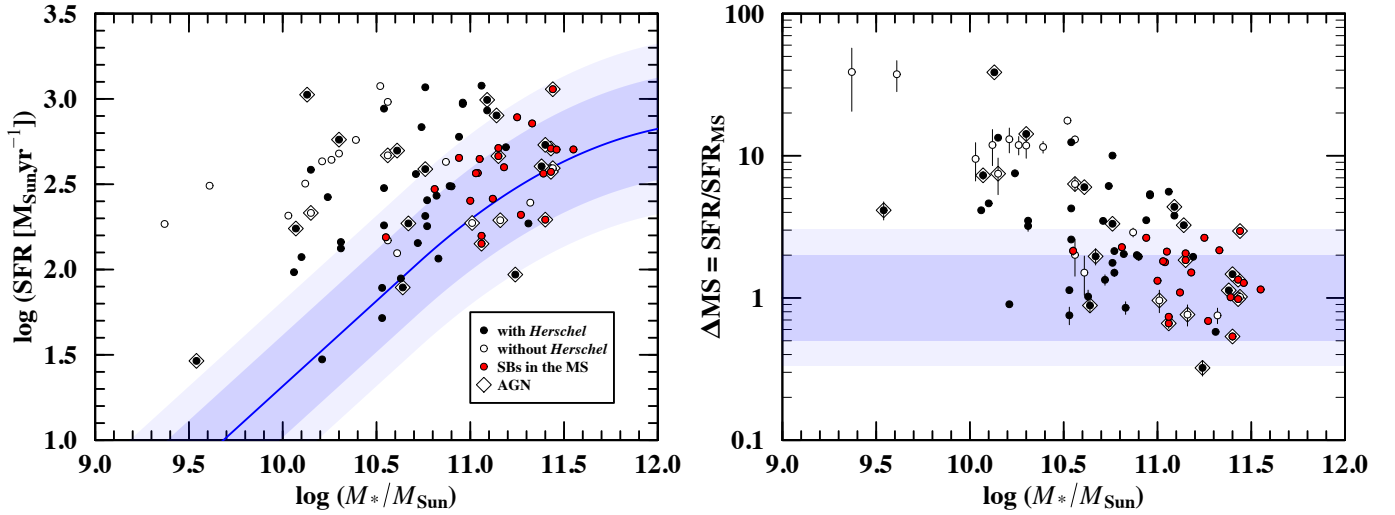


Fig. 2. *Left panel:* SFR– M_* plane with the MS from Schreiber et al. (2015) displayed as a solid blue line. Its 1σ scatter associated with $0.5 < \Delta\text{MS} < 2$ (~ 0.3 dex) is represented as a shaded blue area, with a more extended typical scatter of $0.33 < \Delta\text{MS} < 3$ (~ 0.5 dex) in lighter blue. We note that the values are scaled to a common redshift ($z_{\text{med}} = 2.46$) as explained in the main text. *Right panel:* distance to the MS defined as the ratio of the SFR to the SFR of the MS at a fixed stellar mass and redshift ($\Delta\text{MS} = \text{SFR}/\text{SFR}_{\text{MS}}$). Filled circles represent galaxies with a *Herschel* counterpart and open circles galaxies without a *Herschel* counterpart. SBs in the MS are highlighted in red: galaxies with τ_{dep} below the scatter of the scaling relation and in the MS within a factor 3 (see Sect. 4). Galaxies identified as AGN are highlighted with diamonds.

the median values of the sample ($z_{\text{med}} = 2.46$, $\log(M_{*\text{med}}/M_{\odot}) = 10.79$, and $\Delta\text{MS}_{\text{med}} = 2.15$), keeping constant the distance of the galaxies with respect to the scaling relations of interest. The second and fourth rows offer an alternative representation in terms of the distance of a given property to its scaling relation, defined as the ratio of the property X to the property X in the scaling relation at a fixed redshift, stellar mass and ΔMS ($\Delta X = (X/X_{\text{scI}})$, where $X = \tau_{\text{dep}}$, f_{gas} , and T_{dust}). While the first type of representation (first and third rows) is the most typical, it is again disadvantageous for galaxy samples that span a wide redshift range like ours and, thus, it requires the scaling so that the distance of a given property to the scaling relation is the same as if it was plotted against the scaling relation associated with its redshift, stellar mass, and ΔMS . The alternative representation (second and fourth rows) naturally solves this limitation by plotting directly the distance of a given property to the scaling relation at each galaxy redshift, stellar mass, and ΔMS . We note that in the alternative representation A2GS52 is not displayed in the panels involving $\Delta\tau_{\text{dep}}$, as this galaxy is an outlier with respect to the scaling relation and modifying the y-axis range to include it would result in shrinking too much the rest of the plot to correctly visualize it.

From the $\tau_{\text{dep}}-\Delta\text{MS}$ panel in Fig. 3, there exists a subset of galaxies that exhibit low τ_{dep} , compared to the scaling relation of galaxies at the same redshift, stellar mass, and ΔMS , and located within the scatter of the MS. These characteristics were the ones outlined by Elbaz et al. (2018), along with low f_{gas} and high SFR surface densities, for a population of SBs in the MS. We tagged these galaxies in red following the same definition as Elbaz et al. (2018): SBs in the MS are galaxies with τ_{dep} below the scatter of the scaling relation and in the MS within a factor 3 ($0.33 < \Delta\text{MS} < 3$, 0.5 dex). 23/69 galaxies follow this definition and were classified as SBs in the MS (where the total number of galaxies accounts only for galaxies with a *Herschel* counterpart, as for the remaining galaxies without a *Herschel* counterpart the assessment of whether they were or not SBs in the MS was not possible). We also see that these galaxies with low τ_{dep} and within the scatter of the MS have naturally low f_{gas}

compared to the scaling relation of galaxies at the same redshift, stellar mass, and ΔMS (this is a direct consequence of having low τ_{dep} while being within the scatter of the MS, as low τ_{dep} at constant SFR means low M_{gas}). In addition, they also exhibit anomalously high T_{dust} compared to the scaling relation of galaxies at the same redshift, stellar mass, and ΔMS . Another characteristic is their elevated stellar masses, as the subset of SBs in the MS is on average $\times 2.6$ more massive than the subset of remaining galaxies not labeled as SBs in the MS. Therefore, we conclude that the population of SBs in the MS is characterized by short depletion timescales, low gas fractions, and high dust temperatures in comparison with the scaling relations of galaxies at a fixed redshift, stellar mass, and ΔMS .

AGN as identified in Sect. 3.6 are highlighted with black diamonds in Fig. 3. There is no evidence for correlations between τ_{dep} , f_{gas} , or T_{dust} and AGN activity. Although, a number of galaxies are classified as AGN and it could be a sign of coevolution between AGN and star formation activity, their location in the panels do not follow any particular trend. This is in line with studies indicating the absence of suppression or enhancement of the SFR, dust, or gas masses in AGN hosts at a fixed stellar mass, except for a handful extreme cases (e.g., Valentino et al. 2021).

The distribution of our galaxy sample in Fig. 3 is subject to selection effects. In Sect. 3.7 we introduced the aspects of completeness and selection limits in the GOODS-ALMA 2.0 survey that we now project into Fig. 3. In order to do so, we used the flux density completeness threshold of $S_{1.1\text{mm}} > 1$ mJy for sources with dust continuum sizes up to $1''$ FWHM that defines the GOODS-ALMA 2.0 survey $\sim 100\%$ completeness (see Gómez-Guijarro et al. 2022). We converted this flux density completeness threshold into a M_{dust} limit by using the dust SED template corresponding to the median redshift and ΔMS of our galaxy sample ($z_{\text{med}} = 2.46$ and $\Delta\text{MS}_{\text{med}} = 2.15$), as the values in the panels of the first row were scaled to these medians. Then, the M_{dust} limit was converted into a M_{gas} limit through the $\delta_{\text{GDR}}-Z$ technique where, in this case, the range of stellar masses represented in the x-axis was used to calculate the associated metallicity through MZR and, thus, the associated δ_{GDR} .

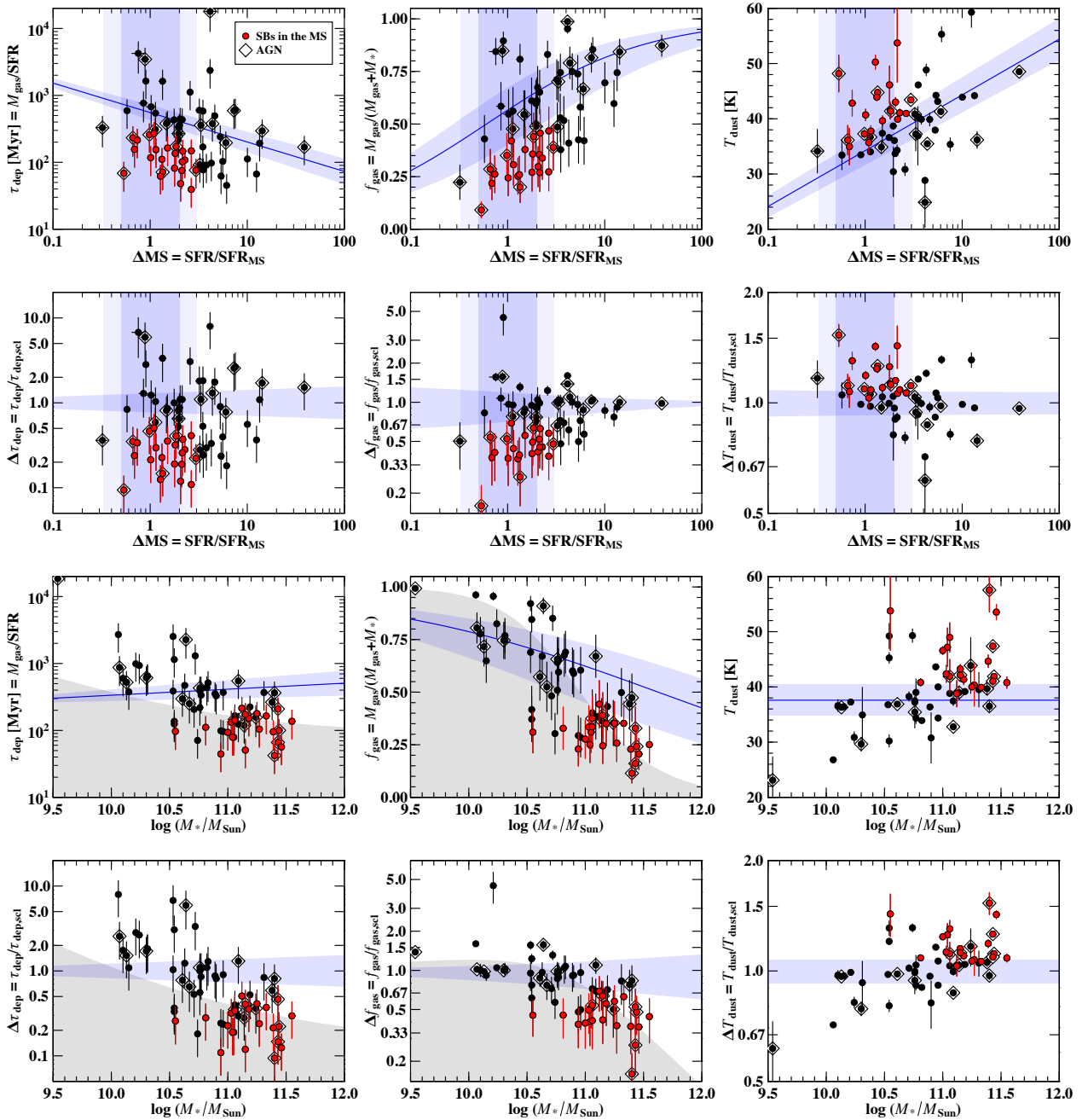


Fig. 3. τ_{dep} (first column), f_{gas} (second column), and T_{dust} (third column) as a function of ΔMS (first row) and stellar mass (third row). Scaling relations for $\tau_{\text{dep}}(z, M_*, \Delta\text{MS})$ and $f_{\text{gas}}(z, M_*, \Delta\text{MS})$ from Tacconi et al. (2018) and for $T_{\text{dust}}(z, \Delta\text{MS})$ from Schreiber et al. (2018) are shown as a solid blue line with their scatter as a shaded blue area. The 1σ scatter of the MS ($0.5 < \Delta\text{MS} < 2$, ~ 0.3 dex) is also shown as a shaded blue area, with a more extended typical scatter of $0.33 < \Delta\text{MS} < 3$ (~ 0.5 dex) in lighter blue (second row). We note that the values are scaled to a common redshift and stellar mass (first row) and to a common redshift and ΔMS (third row) ($z_{\text{med}} = 2.46$, $\log(M_{*,\text{med}}/M_{\odot}) = 10.79$, and $\Delta\text{MS}_{\text{med}} = 2.15$) as explained in the main text. Second and fourth rows: distance of a given property to its scaling relation, defined as the ratio of the property X to the property X in the scaling relation at a fixed redshift, stellar mass and ΔMS ($\Delta X = (X/X_{\text{scl}})$), where $X = \tau_{\text{dep}}$, f_{gas} , and T_{dust} . Only galaxies with a *Herschel* counterpart are displayed. The shaded gray area shows the region where we are no longer $\sim 100\%$ complete (see main text). In all panels, SBs in the MS are in red: galaxies with τ_{dep} below the scatter of the scaling relation and in the MS within a factor 3. Galaxies identified as AGN are highlighted with diamonds.

Therefore, the border of the shaded gray area in the $f_{\text{gas}}-M_*$ panel represents the $\sim 100\%$ completeness threshold and our sample is located alongside it. We see that in the low stellar mass end ($\log(M_*/M_{\odot}) < 10.5$), the selection effects play against finding galaxies below the scaling relation. However, in the high stellar mass end ($\log(M_*/M_{\odot}) > 10.5$) galaxies above and below the scaling relation are within the reach of the survey. At the most

massive end ($\log(M_*/M_{\odot}) > 11.0$), there is a significant excess of galaxies below the scaling relation, which constitute the subset of SBs in the MS, with respect to galaxies above the scaling relation. This is not due to selection effects as galaxies above the scaling relation are favored than galaxies below it in terms of selection effects. Similarly, we project the selection effects into the $\Delta f_{\text{gas}}-M_*$ panel, offering an alternative view.

In the case of τ_{dep} , selection effects are more elusive to be described accurately, as the 1.1 mm flux density completeness threshold better correlates with M_{gas} than with SFR ($\tau_{\text{dep}} = M_{\text{gas}}/\text{SFR}$) for the redshift range of our galaxy sample. M_{gas} is very sensitive to the data points in the RJ side of the IR SED, while SFR is more sensitive to variations in the peak of the dust SED and, thus, T_{dust} . At 1.1 mm, for the redshift range spanned in our galaxy sample, data points are located in the RJ side of the IR SED. Therefore, the limits should be treated as an indication of the regions of the panels subject to incompleteness, but not as an accurate selection function. We converted the flux density completeness threshold into M_{dust} and L_{IR} limits by using the dust SED template corresponding to the median redshift and ΔMS of our galaxy sample. Then, the M_{dust} limit was converted into a M_{gas} limit through the $\delta_{\text{GDR}}-Z$ technique and L_{IR} into SFR to finally get the τ_{dep} limit as a function of stellar mass. We see that in the low stellar mass end ($\log(M_*/M_\odot) < 10.5$), the selection effects play against finding galaxies below the scaling relation. As in the case of f_{gas} , at the most massive end ($\log(M_*/M_\odot) > 11.0$) there exist a significant excess of galaxies below the scaling relation, not due to selection effects, that constitute the subset of SBs in the MS.

Last, for T_{dust} selection effects are more complicated to be described as the 1.1 mm flux density does not correlate with T_{dust} . Nevertheless, selection is more favorable toward colder dust SEDs. A warmer dust SED would require either higher M_{dust} (higher M_{gas} , for a fixed δ_{GDR}) or higher L_{IR} to be detected for a given flux density threshold in the RJ side of the IR SED. We see that in the low stellar mass end ($\log(M_*/M_\odot) < 10.5$), the selection effects play against finding warmer galaxies above the scaling relation. In the most massive end ($\log(M_*/M_\odot) > 11.0$), there exist a significant excess of warmer galaxies above the scaling relation, that constitute the subset of SBs in the MS. This is again not due to selection effects, as colder galaxies below the scaling relation are more favored than warmer galaxies above it.

Appendix C tests the impact of the metallicity assumptions for M_{gas} estimates in the distribution of our galaxy sample in Fig. 3. Figures C.1 and C.2 reproduce Fig. 3 for M_{gas} estimates obtained by using the $\delta_{\text{GDR}}-Z$ with FMR and fixed solar metallicity, respectively. For FMR (solar) the whole distribution shifts to higher (lower) M_{gas} regimes with respect to the gas scaling relations, as expected given the increase (decrease) of δ_{GDR} for metallicities on average lower (higher) through FMR (solar) compare to MZR. We note that both the gas scaling relations and the assessment of selection effects were calculated based on MZR. Nonetheless, the conclusion of the existence of the subset of SBs in the MS remains unchanged. These galaxies are characterized by short depletion timescales, low gas fractions, and high dust temperatures in comparison with the scaling relations of galaxies at a fixed redshift, stellar mass, and ΔMS , regardless of the metallicity assumption for M_{gas} estimates. We note that depending on the metallicity assumption, the subset of SBs in the MS would have slightly varied, as some galaxies enter or exit the selection criteria, that is galaxies with τ_{dep} below the scatter of the scaling relation and in the MS within a factor 3.

5. Compact star formation as a physical driver of depletion timescales, gas fractions, and dust temperatures

We investigated the role of the spatial extent of the ongoing star formation, traced by the dust continuum emission at 1.1 mm linked to the star formation episode and gas reservoir, as a phys-

ical driver of the galaxy sample behavior in relation with the scaling relations shown in the previous section. In particular, we focused on the driver of the anomalous characteristics of the SBs in the MS compared to the scaling relations.

Dust continuum sizes at 1.1 mm for the galaxy sample were presented in Gómez-Guijarro et al. (2022). Briefly, sizes were measured in the uv plane of the GOODS-ALMA 2.0 combined dataset employing the CASA task UVMODELFIT to fit single component models to single sources. We fit a Gaussian model with fixed circular axis ratio, since the scope of the work was to get global size measurements. They were obtained for the galaxies in the 100% pure main catalog (corresponding to ID from A2GS1 to A2GS44), which have a detection $S/N_{\text{peak}} \geq 5$. Measurements below this S/N with a $S/N_{\text{peak}} \leq 5$ were unreliable (corresponding to ID from A2GS45 to A2GS88). In Gómez-Guijarro et al. (2022) we concluded that the galaxy sample dust continuum sizes are generally compact, with a median effective (half-light) radius of $R_e = 0''.10 \pm 0''.05$ and a median physical size of $R_e = 0.73 \pm 0.29$ kpc, calculated at the redshift of each galaxy (where the uncertainties are given by the median absolute deviation). In addition, we concluded that for sources with flux densities $S_{1.1\text{mm}} > 1$ mJy compact dust continuum emission at 1.1 mm prevails, and sizes as extended as typical star-forming stellar disks are rare. For sources with $S_{1.1\text{mm}} < 1$ mJy compact dust continuum emission appears slightly more extended at 1.1 mm, although still generally compact below the sizes of typical star-forming stellar disks.

Among the galaxies for which size measurements were reported in Gómez-Guijarro et al. (2022), a special distinction was made to galaxies with a detection $S/N_{\text{peak}} \geq 6.5$, for which the size measurements were the most reliable (corresponding to ID from A2GS1 to A2GS26). In the following we restricted the analysis to the latter subset. As the size measurements are more reliable with increasing S/N, this choice is a good compromise between using the best size measurements and a sizable sample that includes the sources with flux densities consistent with $S_{1.1\text{mm}} > 1$ mJy, the flux density threshold for which the GOODS-ALMA 2.0 survey reaches a $\sim 100\%$ completeness for sources with dust continuum sizes up to $1''$ FWHM. Therefore, removing galaxies with a detection peak $S/N_{\text{peak}} \leq 6.5$ restricts the analysis to the bright end of the 1.1 mm flux densities where the survey is complete, typically associated with higher M_{gas} galaxies.

In the top row of Fig. 4 we show how τ_{dep} , f_{gas} , and T_{dust} , as derived in Sect. 3, behave as a function of the SFR surface density ($\Sigma_{\text{SFR}} = \text{SFR}/(2\pi R_e^2)$). It is clear that τ_{dep} and T_{dust} correlate with Σ_{SFR} , with higher Σ_{SFR} related to lower τ_{dep} (negative correlation) and higher T_{dust} (positive correlation). Conversely, f_{gas} does not seem to correlate with Σ_{SFR} . These type of relations have been reported by several studies in the literature, both in the case of τ_{dep} (e.g., Elbaz et al. 2018; Franco et al. 2020a) and T_{dust} (Burnham et al. 2021), establishing a physical connection between the increase in Σ_{SFR} and the origin of such relations. However, in order to better establish such physical connections, it is necessary to account for the stellar mass and redshift evolution of the studied properties. In addition, the correlations are at least partially driven by the fact that the studied properties and Σ_{SFR} are related to each other through L_{IR} . Therefore, the drivers of τ_{dep} , f_{gas} , and T_{dust} remain to be understood at a fixed stellar mass and redshift and without invoking related physical quantities.

In the bottom row of Fig. 4 we show the deviations of τ_{dep} , f_{gas} , and T_{dust} compared to the gas scaling relations of normal MS SFGs ($\Delta\text{MS} = 1$) in relation to the

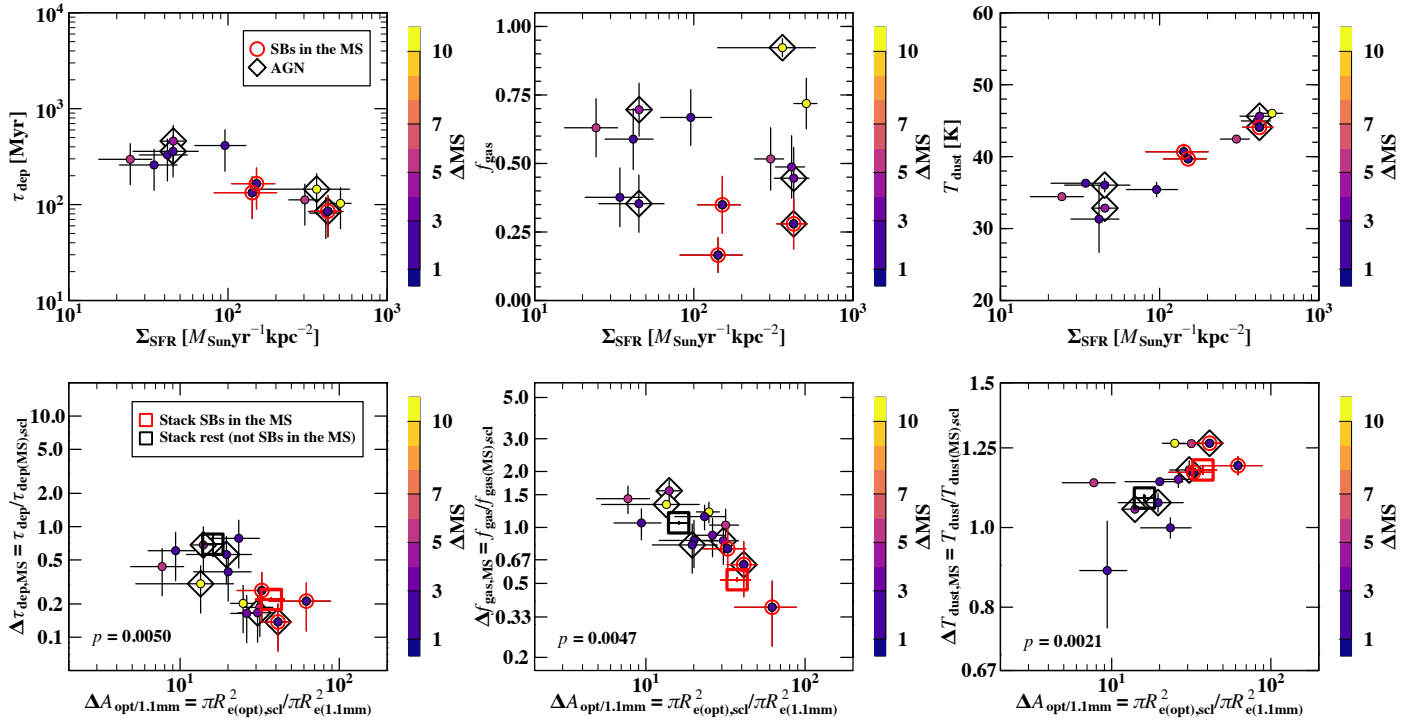


Fig. 4. *Top row:* τ_{dep} (first column), f_{gas} (second column), and T_{dust} (third column) as a function of Σ_{SFR} . Only galaxies with a *Herschel* counterpart with the most reliable size measurements in Gómez-Guijarro et al. (2022) are shown (corresponding to a detection $S/N_{\text{peak}} \geq 6.5$). SBs in the MS are in red. Galaxies identified as AGN are highlighted with diamonds. All galaxies are color coded according to their ΔMS . *Bottom row:* deviations of τ_{dep} (first column), f_{gas} (second column), and T_{dust} (third column) compared to the gas scaling relations of normal MS SFGs ($\Delta\text{MS} = 1$) in relation with the deviations of the dust continuum areas compared to the structural scaling relation of normal SFGs at a fixed stellar mass and redshift. The gas scaling relations for $\tau_{\text{dep}}(z, M_*, \Delta\text{MS})$ and $f_{\text{gas}}(z, M_*, \Delta\text{MS})$ are from Tacconi et al. (2018), and for $T_{\text{dust}}(z, \Delta\text{MS})$ from Schreiber et al. (2018), where $\Delta\text{MS} = 1$. In the case of the structural scaling relation, we compared the dust continuum areas with the typical areas of star-forming stellar disks measured at optical wavelengths for late-type galaxies from van der Wel et al. (2014), at a fixed stellar mass and redshift. The stack of the 23/69 galaxies that were classified as SBs in the MS originally in Fig. 3 is shown as an empty red square (where the total number of galaxies accounts only for galaxies with a *Herschel* counterpart). Similarly, the stack of the remaining galaxies that were not labeled as SBs in the MS in Fig. 3 are shown as an empty black square.

deviations of the dust continuum sizes compared to the structural scaling relation of normal SFGs at the same stellar mass and redshift. In the case of the gas scaling relations, we compared them with those established in the literature for $\tau_{\text{dep}}(z, M_*, \Delta\text{MS})$ and $f_{\text{gas}}(z, M_*, \Delta\text{MS})$ from Tacconi et al. (2018), and for $T_{\text{dust}}(z, \Delta\text{MS})$ from Schreiber et al. (2018), as in Sect. 4, where $\Delta\text{MS} = 1$ in this case. Regarding the structural scaling relation, we compared the dust continuum sizes with the typical size of star-forming stellar disks measured at optical wavelengths for late-type galaxies from van der Wel et al. (2014) at the same stellar mass and redshift. In Gómez-Guijarro et al. (2022) we found that dust continuum sizes evolve with redshift and stellar mass resembling the trends of the stellar sizes measured at optical wavelengths, albeit a lower normalization compared to those of late-type galaxies. The outlined approach permits to study the relation of a geometrical property like the sizes of the ongoing star formation regions with the physical properties of the galaxies in terms of their τ_{dep} , f_{gas} , and T_{dust} , at a fixed stellar mass and redshift. We note that in the case of the sizes we used areas instead of one-dimensional sizes. Also we note that the definition of the deviations of the dust continuum areas compared to the structural scaling relation of normal SFGs at the fixed stellar mass and redshift is given by $\Delta A = (\pi R_{\text{e(opt),scl}}^2 / \pi R_{\text{e(1.1mm)}}^2)$, so that increasing compact star formation with respect to typical sizes of star-forming stellar disks is associated with increasing values in the x -axis.

Dust continuum areas at 1.1 mm (dust compactness) with respect to the typical size of star-forming stellar disks (measured at optical wavelengths) appear to be correlated with τ_{dep} , f_{gas} , and T_{dust} . As dust continuum becomes more compact with respect to typical sizes of star-forming stellar disks, τ_{dep} and f_{gas} become lower and T_{dust} higher compared to the gas scaling relations of normal MS SFGs, at a fixed stellar mass and redshift.

In order to study whether there exist formal correlations, we performed statistical simulations of the nonparametric Spearman rank correlation test. We followed a bootstrapping approach generating 100 000 simulations of the galaxy sample. In other words, for each of the statistical simulations we generated a sample of galaxies allowing replacements of the same number of galaxies as the original sample and calculated the Spearman's rank correlation coefficient (r_s). This approach ensures that single points are not the sole drivers of a potential correlation, as points are included and removed randomly in the different realizations studying the existence of a correlation each time. The probability of no correlation (p -value) is given by the number of simulations for which $r_s < 0$, for a positive correlation, or $r_s > 0$, for a negative correlation (multiplied by two since it is a bilateral test). The probabilities of no correlation are 0.50%, 0.47%, and 0.21% (p -value) for τ_{dep} , f_{gas} , and T_{dust} , respectively. This confirms correlations for τ_{dep} , f_{gas} , and T_{dust} (considering rejections at 5%).

Figure 5 summarizes in a simple drawing the results from our observations in terms of the gas fraction. The less amount

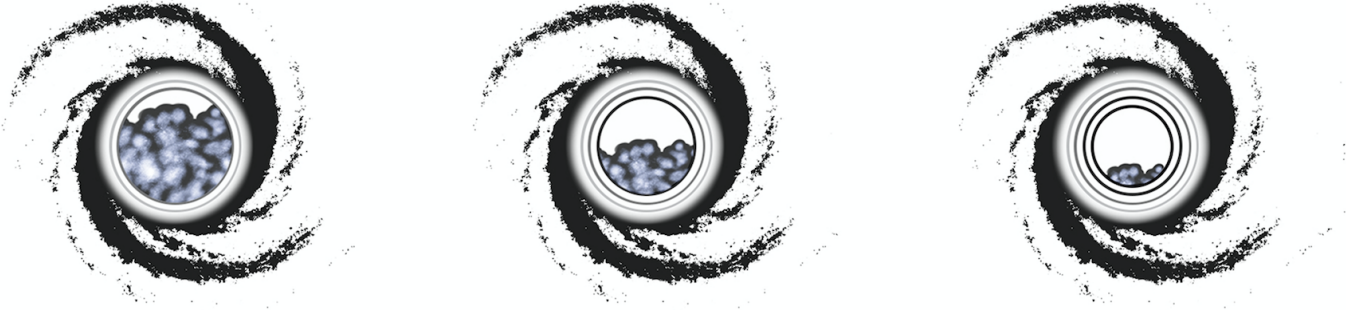


Fig. 5. Drawing summarizing the results from our observations in terms of the gas fraction. From left to right, the less amount of gas in the galaxy (represented as a shrinking blue region), the more compact the star-forming region becomes (represented as a shrinking inner black circle).

of gas in the galaxy (represented as the shrinking blue region), the more compact the star-forming region becomes (represented as the shrinking inner black circle). We note that this drawing is aimed to be a simple representation of the trend involving f_{gas} in Fig. 5 in the $\Delta f_{\text{gas,MS}} - \Delta A_{\text{opt}/1.1\text{mm}}$ plane, but it is not aimed to be a representation of what could be the physical processes necessary for this compression to happen or about the externally and/or internally-driven morphological transformations involved in the process.

Another interesting aspect in Fig. 4 is that, when comparing the top and bottom rows, SBs in the MS move to the extremes of the trends. SBs in the MS appear to be the extreme cases where the dust continuum areas are the most compact ones compared to the structural scaling relation for typical star-forming stellar disks. They are associated with the lowest τ_{dep} and f_{gas} , and the highest T_{dust} compared to the gas scaling relations for normal MS SFGs at a fixed stellar mass and redshift.

However, our galaxy sample of SBs in the MS in Fig. 4 is scarce. Given that SBs in the MS are characterized by depleted f_{gas} , it could be that they had a low surface brightness extension of the dust continuum emission not properly captured in the size measurements for individual galaxies. In order to verify the latter, we stacked the 1.1 mm data for all the 23/69 galaxies that were classified as SBs in the MS originally in Fig. 3 (where the total number of galaxies accounts only for galaxies with a *Herschel* counterpart). In addition, we stacked the 1.1 mm data for the remaining galaxies that were not labeled as SBs in the MS in Fig. 3. The stacks were performed in the uv plane following the methodology described in Gómez-Guijarro et al. (2022) for uv plane stacking. We measured the sizes of the stacks employing the Common Astronomy Software Applications (CASA; McMullin et al. 2007) task UVMODELFIT, fitting a Gaussian model with fixed circular axis ratio as in Gómez-Guijarro et al. (2022). In the bottom row of Fig. 4 we show in the x -axis dust continuum areas resulting from these stacks and in the y -axis median values for τ_{dep} , f_{gas} , and T_{dust} for both SBs in the MS (red) and the remaining galaxies (black). We note that the deviations compared to the scaling relations were evaluated at the median redshift and stellar mass of each subset. These values are in agreement with the correlations drawn from the individual galaxies as explained above.

In Gómez-Guijarro et al. (2022) we found that dust continuum sizes evolve with redshift and stellar mass resembling the trends of the stellar sizes measured at optical wavelengths. As mentioned in Sect. 4, the subset of SBs in the MS is on average $\times 2.6$ more massive than the subset of remaining galaxies not labeled as SBs in the MS. The median redshifts and stellar masses of the SBs in the MS are $z = 2.36 \pm 0.05$ and

$\log(M_*/M_\odot) = 11.15 \pm 0.01$, while for the remaining galaxies are $z = 2.17 \pm 0.02$ and $\log(M_*/M_\odot) = 10.73 \pm 0.01$. The representation of the bottom row of Fig. 4 naturally accounts for these differences by plotting directly the deviation of a given property to the scaling relation at a fixed redshift and stellar mass. But if sizes as given by the effective radius were to be compared, they need to be expressed in the same terms of redshift and stellar mass. We corrected the dust continuum sizes of the stacks to a common redshift and stellar mass, as given by the median values of our galaxy sample ($z_{\text{med}} = 2.46$ and $\log(M_{* \text{med}}/M_\odot) = 10.79$), by using the $R_c(z, M_*)$ dependency of late-type galaxies of van der Wel et al. (2014). The stack of SBs in the MS with a dust continuum size of $R_c^{\text{cor}} = 0.52 \pm 0.05$ kpc is indeed more compact than the stack of the remaining galaxies that were not labeled as SBs in the MS, with a dust continuum size of $R_c^{\text{cor}} = 0.99 \pm 0.06$ kpc.

Selection effects are at play in Fig. 4 and could potentially affect the correlations found. In general, as GOODS-ALMA 2.0 is a flux limited survey, for a fixed flux density threshold detections are biased against more extended sources. Therefore, the selection effects in Fig. 4 would miss more extended and gas poor galaxies that could potentially populate the bottom-left area in the τ_{dep} and f_{gas} panels. Similarly, as cold galaxies are also favored, selection effects would miss more extended and warm galaxies that could populate the top-left area in the T_{dust} panel. Nonetheless, as the opposite corners of the three panels are not subject to these selection effects, the most compact galaxies would still have lower τ_{dep} and f_{gas} , and higher T_{dust} compared to the gas scaling relations of normal MS SFGs, at a fixed stellar mass and redshift. In addition, it is important to note that the galaxies represented in Fig. 4 have flux densities $S_{1.1\text{mm}} > 1$ mJy, the flux density threshold for which the GOODS-ALMA 2.0 survey reaches a $\sim 100\%$ completeness for sources with dust continuum sizes up to $1''$ FWHM. In Gómez-Guijarro et al. (2022) we concluded that for sources with flux densities $S_{1.1\text{mm}} > 1$ mJy compact dust continuum emission at 1.1 mm prevails, and sizes as extended as typical star-forming stellar disks are rare. Therefore, it is not expected that in the $S_{1.1\text{mm}} > 1$ mJy flux density regime included in Fig. 4 the selection function depends on the size. In Gómez-Guijarro et al. (2022), for sources with $S_{1.1\text{mm}} < 1$ mJy, compact dust continuum emission appeared slightly more extended at 1.1 mm, although still generally compact below the sizes of typical star-forming stellar disks. In this flux density regime, it would be plausible to find more extended galaxies populating the areas toward lower values in the x -axis in all the panels of Fig. 4. It is also plausible to image some cases of outliers, while not violating the causes outlined by the correlations. For example, two

merging galaxies that have not yet reached coalescence would appear more extended than what would correspond to the correlations, but not necessarily reflect variations in τ_{dep} , f_{gas} , or T_{dust} . Another case also related would be an already ignited starburst episode, reflecting shorter τ_{dep} and higher T_{dust} than the scaling relations, which could also appear more extended and more gas rich than what would correspond to the correlations if it was receiving an extra gas supply from another merging galaxy that has not yet reached coalescence.

Recent studies by Jin et al. (2019) and Cortzen et al. (2020) have shown evidence for deceptively cold T_{dust} in massive starbursts at $z > 3$ derived under the common assumption of an optically thin far-IR dust emission. Conversely, when a general opacity solution was applied, the authors found warmer temperatures fully consistent with the excitation temperatures from far-IR lines. The authors concluded that the presence of optically thick dust up to longer wavelengths than the classical thin assumptions lead to, not only a systematic underestimation of T_{dust} , but also an overestimation of M_{dust} and, thus, M_{gas} for a fixed δ_{GDR} . While the more compact the dust emitting region the more likely is to be optically thick up to longer wavelengths, the high T_{dust} estimates for our subset of SBs in the MS point to a correct opacity assumption. Even if the latter was not the case, a general opacity solution would lead to lower M_{gas} estimates, strengthening our conclusions.

In a similar way to the test introduced in the previous section, Appendix C tests the impact of the metallicity assumptions for M_{gas} estimates in the distribution of our galaxy sample in Fig. 4. Figures C.3 and C.4 reproduce Fig. 4 for M_{gas} estimates obtained by using the $\delta_{\text{GDR}}-Z$ with FMR and fixed solar metallicity, respectively. The correlations still hold regardless of the metallicity assumption for M_{gas} estimates (except in the case of τ_{dep} for fixed solar metallicity, although it is only due to one outlier). Besides, in all cases SBs in the MS move to the extremes of the trends.

Last, in the case of AGN there is no evidence for a correlation between the properties displayed in Fig. 4 and AGN activity, as their location in the panels is not particularly linked to a specific region of the plot or to the SBs in the MS preferentially respect to the remaining galaxies that were not labeled as SBs in the MS.

6. Discussion

In this section we interpret the results presented in the previous sections in the global picture of galaxy evolution. The scope of this discussion is to compare the expectations of common scenarios for galaxy evolution with our observations to verify up to what degree they are able to explain our measurements and whether updated scenarios need to be introduced to explain all the results presented in previous sections.

As outlined in Sect. 1, the MS of SFGs and, in particular, its small scatter suggests that secular evolution is the dominant mode of stellar assembly. In this picture, gas inflows, outflows, and consumption in star formation are in a steady equilibrium regulating galaxy evolution (e.g., Daddi et al. 2010; Genzel et al. 2010; Tacconi et al. 2010; Dekel et al. 2013; Feldmann & Mayer 2015). As a result, SFGs would spend most of their time evolving as extended star-forming disks. Conversely, QGs are located below the MS and are typically more compact than SFGs at a fixed stellar mass and redshift (e.g., Shen et al. 2003; van der Wel et al. 2014; Barro et al. 2017; Suess et al. 2019; Mowla et al. 2019). Therefore, the quenching of star forma-

tion appears to involve the build-up of a central stellar core (e.g., Kauffmann et al. 2003; Whitaker et al. 2017; Barro et al. 2017; Gómez-Guijarro et al. 2019; Suess et al. 2021). Optically compact MS SFGs have been proposed as the missing link between the SFGs and the more compact QGs, as they exhibit star formation consistent with the trends of more extended MS SFGs, but with a stellar structure comparable to QGs (e.g., Barro et al. 2013; Nelson et al. 2014; Williams et al. 2014; van Dokkum et al. 2015; Gómez-Guijarro et al. 2019). Other recent works have also indicated the existence of galaxies that exhibit compact emission in several far-IR tracers, such as dust continuum at submm/mm and radio wavelengths or CO lines, while located within the scatter of the MS (e.g., Elbaz et al. 2018; Jiménez-Andrade et al. 2019; Puglisi et al. 2019, 2021; Franco et al. 2020a). However, the origin, nature, and role in galaxy evolution of these different types of compact MS SFGs galaxies remains to be understood.

On one hand, several studies have advocated for compaction events predicted by galaxy formation models in which extended MS SFGs can secularly evolve into compact MS SFGs by funneling gas to their central regions yielding the build up of their stellar cores (e.g., Dekel et al. 2013; Zolotov et al. 2015; Tacchella et al. 2016). In particular Tacchella et al. (2016) describes this scenario as the following (Scenario 1, Fig. 6, left panel): an intense gas inflow event triggers the so-called compaction event, involving counter-rotating streams or minor mergers, and is commonly associated with violent disk instabilities. The inflow rate is more efficient than the SFR. The gas is funneled to the center of the galaxy and a compact massive core of gas and star formation rate develops. This phase is characterized by a short depletion time and a high gas fraction. Subsequently, the galaxy moves to the upper bound of the MS scatter and the downturn is associated with the peak of SFR and outflow and the suppression of the inflow. Consequently, central gas depletion leads to inside-out quenching and the galaxy moves to the lower bound of the MS scatter. At low masses, the dark matter halo is still cold and gas inflow is resumed and subsequent compaction events follow. At high masses, the hot dark matter halo prevents further gas inflow, leading to gas depletion and full quenching.

On the other hand, other studies have advocated that SBs dominated by a violent episode of star formation typical of gas-rich mergers are also capable of funneling gas to the center of collision and quickly build up compact stellar cores (e.g., Mihos & Hernquist 1996; Hopkins et al. 2006; Toft et al. 2014; Gómez-Guijarro et al. 2018; Puglisi et al. 2021). In this case (Scenario 2, Fig. 6, middle panel): an extra supply of gas comes from gas-rich galaxy mergers that efficiently dissipate angular momentum. The gas is funneled to the center of collision, becomes denser, and star formation is enhanced. As a result, the galaxy moves well above the MS. Subsequently, it falls toward the MS when the SFR declines as the gas reservoir is consumed. Finally, the galaxy crosses the MS toward quiescence. SBs in the MS would be galaxies on their way to quiescence, incidentally in the MS, but without being part of it (e.g., Elbaz et al. 2018; Gómez-Guijarro et al. 2019; Puglisi et al. 2021).

Our findings are more in line with Scenario 2. In particular, the characteristics of the SBs in the MS, exhibiting the most compact star formation, shortest depletion times, lowest gas fractions (and highest dust temperatures) of our galaxy sample. These characteristics point toward SBs in the MS as a stage prior to passivization that could potentially evolve into optically compact MS SFGs once the central stellar core is built up and eventually quench forming QGs. Conversely, in Scenario 1,

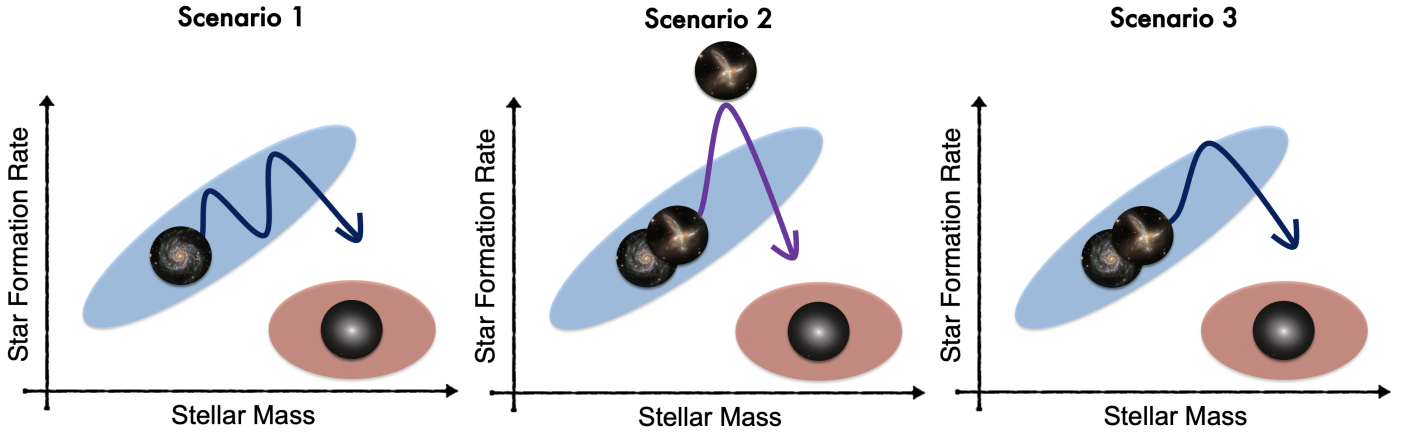


Fig. 6. Drawing depicting possible scenarios of galaxy evolution in the main sequence framework. Scenario 1 (*left panel*): external gas inflow triggers a compaction event. The gas is funneled to the center of the galaxy and it moves to the upper bound of the MS. This phase is characterized by a compact core with a high f_{gas} , high SFR, and low τ_{dep} , compared to normal MS SFGs at a fixed stellar mass and redshift. Central gas depletion leads to inside-out quenching and the galaxy moves to the lower bound of the MS. This implies that when MS SFGs have low f_{gas} , they exhibit a more extended star-forming region in comparison to the previous phase. Scenario 2 (*middle panel*): external gas supply from gas-rich mergers. The gas is funneled to the center of collision, enhances SFR, and the galaxy moves well above the MS. As the gas reservoir is consumed, the SFR declines and the galaxy crosses, incidentally, the MS. Scenario 3 (*right panel*): angular momentum loss is driven externally (accretion through mergers or counter-rotating streams) or internally (clump migration). The gas is funneled to the center of the galaxy in either case (represented by a merger in the panel), enhances SFR (although not necessarily directly or well above the MS in all cases). As the gas reservoir is consumed the star-forming region becomes more compact sustaining the SFR (outside-in gas consumption). In all three scenarios, the assumption is that at high masses the hot dark matter halo prevents further gas inflow and the galaxy eventually quenches.

gas-depleted galaxies in the lower bound of the MS should be more extended than those in the upper bound as the gas is centrally depleted. Besides, we do not find galaxies characterized simultaneously by ongoing compact star formation, short depletion times, high gas fractions, and located within the scatter of the MS, as predicted in Scenario 1 in the upper bound of the MS.

Selection effects described in previous sections are at play. In the low stellar mass end ($\log(M_*/M_\odot) < 10.5$), the selection effects act in favor of finding galaxies above the scaling relation in the $f_{\text{gas}}-M_*$ plane, but against finding galaxies below the scaling relation in the $\tau_{\text{dep}}-M_*$ plane. In the high stellar mass end ($\log(M_*/M_\odot) > 10.5$) galaxies above and below the scaling relations are within the reach of the survey. Therefore, galaxies characterized simultaneously by ongoing compact star formation, short depletion times, high gas fractions, and located within the scatter of the MS (as predicted in Scenario 1 in the upper bound of the MS), although not present in the high mass end, they could still exist in the low stellar mass end but remain out of reach to our survey. We note that the interpretation outlined in this discussion is, therefore, to be suitable in the high stellar mass end. In this massive regime, we assumed that quenching proceeds providing that gas replenishment is halted or strongly suppressed, following studies that indicated that the hot dark matter halo at high masses prevents further gas inflow and/or gas cooling leading to gas depletion and full quenching (e.g., Rees & Ostriker 1977; Birnboim & Dekel 2003; Feldmann & Mayer 2015).

An aspect to consider is that in both Scenario 1 and Scenario 2 the loss of angular momentum to compact the galaxy comes from an externally-driven process, invoking counter-rotating streams or mergers. Some studies have indicated that internally-driven processes can also compact the galaxy, such as violent instabilities in gas-rich systems at high redshift that create giant clumps that migrate to the center of the galaxy (e.g., Elmegreen et al. 2008). In addition, feedback-induced turbulence in a SB is a proposed mechanism to self-regulate star formation in these systems (e.g., Ostriker & Shetty 2011;

Lehnert et al. 2013; Brucey et al. 2020), so the extra supply of gas from gas-rich galaxy mergers could not always result in enhanced star formation or the enhancement could be delayed. In Fig. 3 we see that there are some galaxies above the scaling relation in the $f_{\text{gas}}-M_*$ within the scatter of the MS and, simultaneously, above the scaling relation in the $\tau_{\text{dep}}-M_*$ plane. Galaxies of this kind were found by Kokorev et al. (2021), so-called gas giants, and their nature is still to be confirmed. They could be candidates to galaxies in which SFR is not enhanced, either caught in an early phase before doing so or self-regulated by their own feedback-driven turbulence.

Another important aspect to be considered are our findings in Sect. 5 depicting correlations between the physical extent of the dust continuum areas and the deviations from the gas scaling relations. In Fig. 4 we showed that as dust continuum areas become more compact compared to the structural scaling relation of typical star-forming stellar disks, τ_{dep} and f_{gas} become lower and T_{dust} higher compared to the gas scaling relations of normal MS SFGs, at a fixed stellar mass and redshift. In addition, SBs in the MS appear to be the extreme cases where the dust continuum areas are the most compact ones, associated with the lowest τ_{dep} and f_{gas} , and the highest T_{dust} . In particular, it is important to note the result in terms of the gas fraction depicted in Fig. 5, reflecting that the less amount of gas in the galaxy, the more compact the star-forming region becomes. Moreover, SBs in the MS form a high fraction of the subset of the most massive galaxies in the sample ($\log(M_*/M_\odot) > 11.0$), accounting for 59% (19/32, where the total number of galaxies accounts only for galaxies with a *Herschel* counterpart in that mass regime).

These aspects appear to imply that the SFR is somehow sustained, keeping galaxies within the MS even when the f_{gas} is low in very massive systems, presumably on their way to quiescence. It seems that gas and star formation compression allows to hold the SFR. While the specific physical mechanism at play is beyond the scope of this paper, it could be plausible to think that as the gas is funneled to the central regions and stars are formed at the core, the potential well gets steeper and, provided

Table 3. Summary of expectations and observations for the different scenarios of galaxy evolution in the main sequence framework.

	Expected	Observed
Scenario 1	In the MS higher gas content related to more compact star-forming region than lower gas content.	In the MS the lowest gas content related to the most compact star-forming region.
Scenario 2	Compact star-forming region well above the MS related to higher gas content and in the MS related to lower gas content.	In the MS the lowest gas content related to more compact star-forming region than well above the MS with higher gas content.
Scenario 3	In the MS higher gas content related to more extended star-forming region than lower gas content. The less amount of gas in the galaxy, the more compact the star-forming region becomes.	

Notes. This table summarizes the main expectations and some important observed aspects with respect to the gas content and the sizes of the star-forming regions. We note that for Scenario 3 expectations and observations are the same, as this scenario is motivated to match the observations in this work.

angular momentum is lost, gas could be funneled progressively more and more to the core.

In the latter case, there is one point to be considered for galaxies with enhanced star formation that move well above the MS and, subsequently, fall toward the MS when the SFR is declined as their gas reservoir is consumed. They would slow down in their descent as the gas and star formation are compressed and the SFR held, in comparison to the case in which the gas is consumed but without compression. In Fig. 4 we see that this could be the case judging from the relative locations of SBs well above the MS ($\Delta_{\text{MS}} > 10$, yellow points) compared to SBs in the MS in the $\Delta f_{\text{gas,MS}} - \Delta A_{\text{opt}/1.1\text{mm}}$ plane. SBs well above the MS appear more extended compared to SBs in the MS. However, at the moment the sample size for both SBs in the MS and SBs above the MS in this diagram is scarce to draw strong conclusions.

All together, an alternative scenario could be at play (Scenario 3, Fig. 6, right panel): angular momentum loss is driven either externally (accretion through mergers or counter-rotating streams) or internally (clump migration). The gas is funneled to the center in either case (represented by a merger in Fig. 6, right panel) and star formation enhanced, although not necessarily directly or well above the MS in all cases. In any case, as the gas reservoir is consumed, the star-forming region becomes more compact sustaining the SFR (outside-in gas consumption). The galaxy would spend more time on average within the MS compared to that of Scenario 2. SBs in the MS would be galaxies on their way to quiescence, but still experiencing the last phases of regulation implied by the MS.

Scenario 3 is consistent with a slow downfall (e.g., Schreiber et al. 2016; Gómez-Guijarro et al. 2019; Franco et al. 2020a), in which galaxies seem to progressively reduce their f_{gas} and SFR as they assemble their stellar masses and build-up their compact stellar cores. Last, far-IR compact MS SFGs exhibit properties that resemble those of SBs, such as higher gas densities and more excited spectral line energy distributions compared to normal MS SFGs (Puglisi et al. 2021). Optically compact SFGs exhibit far-IR and radio properties consistent with being old SBs winding down compared to normal MS SFGs (Gómez-Guijarro et al. 2019). Both Scenarios 2 and 3 could explain these characteristics. In particular, in the case of Scenario 3 it would mean that as star formation becomes more compact it acts effectively as a central starburst.

A summary of each scenario is provided in Fig. 6 and its caption. Table 3 provides a summary of what the expectations are

of the different scenarios compared to some important observed features in this work. Note also that not all aspects of the scenarios are mutually exclusive. In terms of the low gas fraction phase, Scenario 1 would lead to a more extended star-forming region configuration excluded in Scenarios 2 and 3. In the case of Scenarios 2 and 3, both lead to a more compact star-forming region associated with the low gas fraction phase, but Scenario 3 includes the fact that it would be the most compact, even more compact than SBs above the MS to reproduce the correlation found. In terms of the mechanism triggering compact star formation, both Scenarios 1 and 2 invoke external processes. In the case of Scenario 1, these are predominately accretion-driven counter rotating streams or minor mergers. Scenario 2 instead alludes to the importance of gas-rich mergers. Scenario 3 alludes to the possibility of both external and internal processes, as the observables studied in this work do not preferentially point to either of them, and both seem plausible according to literature studies.

7. Summary and conclusions

In this work we follow up on the galaxy sample presented in Gómez-Guijarro et al. (2022) from the GOODS-ALMA 2.0 survey, an ALMA blind survey at 1.1 mm covering a contiguous area of 72.42 arcmin² using two array configurations at a similar and homogeneous depth over the whole field. The combined mosaic with both configurations reaches an average sensitivity of 68.4 $\mu\text{Jy beam}^{-1}$ at an average angular resolution of $0''.447 \times 0''.418$. We present the dust and stellar-based properties of the galaxy sample. In particular, we study the physical properties of the galaxies in the framework of the main sequence and the scaling relations for depletion timescales, gas fractions, and dust temperatures. We focus on the role of compact star formation traced by the dust continuum emission as a physical driver of the galaxies properties, and on the origin, nature, and role of starburst galaxies located within the main sequence of SFGs. In summary we find:

- There exist a subset of galaxies that exhibit short depletion timescales compared to typical SFGs at the same redshift, stellar mass, and distance to the main sequence. At the same time, these galaxies are located within the scatter of the main sequence. Therefore, we describe these galaxies as starbursts in the main sequence.
- Starbursts in the main sequence are characterized by short depletion timescales, low gas fractions, and high dust

temperatures in comparison with typical main sequence galaxies at the same stellar mass and redshift. They also exhibit high stellar masses, accounting for 59% of the most massive galaxies in the sample ($\log(M_*/M_\odot) > 11.0$).

- Dust continuum areas at 1.1 mm appear to correlate with depletion timescales, gas fractions, and dust temperatures. As galaxies become more compact compared to typical SFGs stellar disks, depletion timescales and gas fractions become lower, and dust temperatures higher, compared to typical main sequence SFGs, at the same stellar mass and redshift. These trends manifest a direct link between a geometrical property like the sizes of the ongoing star formation regions and other physical properties of the galaxies.
- Starbursts in the main sequence appear to be located at the extremes of the trends, reflecting that they are extreme cases where the dust continuum areas are the most compact ones, associated with the shortest depletion timescales, lowest gas fractions, and the highest dust temperatures, compared to typical main sequence SFGs at the same stellar mass and redshift.

Our findings suggest that the star formation rate is somehow sustained in very massive SFGs, keeping them within the main sequence even when their gas fractions are low and they are presumably on their way to quiescence. It seems that gas and star formation compression allows to hold their star formation rate.

Acknowledgements. V.I.K. and G.E.M. acknowledge the Villum Fonden research grant 13160 “Gas to stars, stars to dust: tracing star formation across cosmic time” and the Cosmic Dawn Center of Excellence funded by the Danish National Research Foundation under the grant No. 140. M.T.S. acknowledges support from a Scientific Exchanges visitor fellowship (IZSEZO_202357) from the Swiss National Science Foundation. M.F. acknowledges the support from STFC (grant number ST/R000905/1). H.I. acknowledges support from JSPS KAKENHI Grant Number JP19K23462 and JP21H01129. This paper makes use of the following ALMA data: ADS/JAO.ALMA#2015.1.00543.S and ADS/JAO.ALMA#2017.1.00755.S. ALMA is a partnership of ESO (representing its member states), NSF (USA) and NINS (Japan), together with NRC (Canada), MOST and ASIAA (Taiwan), and KASI (Republic of Korea), in cooperation with the Republic of Chile. The Joint ALMA Observatory is operated by ESO, AUI/NRAO and NAOJ. We are grateful to the anonymous referee, whose comments have been very useful to improve our work.

References

- Barro, G., Faber, S. M., Pérez-González, P. G., et al. 2013, *ApJ*, 765, 104
- Barro, G., Faber, S. M., Koo, D. C., et al. 2017, *ApJ*, 840, 47
- Berta, S., Lutz, D., Genzel, R., Förster-Schreiber, N. M., & Tacconi, L. J. 2016, *A&A*, 587, A73
- Béthermin, M., Daddi, E., Magdis, G., et al. 2015, *A&A*, 573, A113
- Birnboim, Y., & Dekel, A. 2003, *MNRAS*, 345, 349
- Boogaard, L. A., Decarli, R., González-López, J., et al. 2019, *ApJ*, 882, 140
- Brammer, G. B., van Dokkum, P. G., & Coppi, P. 2008, *ApJ*, 686, 1503
- Brammer, G. B., Whitaker, K. E., van Dokkum, P. G., et al. 2011, *ApJ*, 739, 24
- Brammer, G. B., van Dokkum, P. G., Franx, M., et al. 2012, *ApJS*, 200, 13
- Brinchmann, J., Charlot, S., White, S. D. M., et al. 2004, *MNRAS*, 351, 1151
- Brucy, N., Hennebelle, P., Bournaud, F., & Colling, C. 2020, *ApJ*, 896, L34
- Bruzual, G., & Charlot, S. 2003, *MNRAS*, 344, 1000
- Burnham, A. D., Casey, C. M., Zavala, J. A., et al. 2021, *ApJ*, 910, 89
- Calzetti, D., Armus, L., Bohlin, R. C., et al. 2000, *ApJ*, 533, 682
- Cardamone, C. N., van Dokkum, P. G., Urry, C. M., et al. 2010, *ApJS*, 189, 270
- Chabrier, G. 2003, *PASP*, 115, 763
- Cibinel, A., Daddi, E., Sargent, M. T., et al. 2019, *MNRAS*, 485, 5631
- Condon, J. J. 1992, *ARA&A*, 30, 575
- Coogan, R. T., Sargent, M. T., Daddi, E., et al. 2019, *MNRAS*, 485, 2092
- Cortzen, I., Magdis, G. E., Valentino, F., et al. 2020, *A&A*, 634, L14
- da Cunha, E., Charlot, S., & Elbaz, D. 2008, *MNRAS*, 388, 1595
- Daddi, E., Cimatti, A., Renzini, A., et al. 2004, *ApJ*, 617, 746
- Daddi, E., Dickinson, M., Morrison, G., et al. 2007, *ApJ*, 670, 156
- Daddi, E., Dannerbauer, H., Elbaz, D., et al. 2008, *ApJ*, 673, L21
- Daddi, E., Bournaud, F., Walter, F., et al. 2010, *ApJ*, 713, 686
- Davidzon, I., Ilbert, O., Laigle, C., et al. 2017, *A&A*, 605, A70
- Decarli, R., Walter, F., González-López, J., et al. 2019, *ApJ*, 882, 138
- de Jong, T., Klein, U., Wielebinski, R., & Wunderlich, E. 1985, *A&A*, 147, L6
- Dekel, A., Zolotov, A., Tweed, D., et al. 2013, *MNRAS*, 435, 999
- Del Moro, A., Alexander, D. M., Mullaney, J. R., et al. 2013, *A&A*, 549, A59
- Delvecchio, I., Smolčić, V., Zamorani, G., et al. 2017, *A&A*, 602, A3
- Delvecchio, I., Daddi, E., Sargent, M. T., et al. 2021, *A&A*, 647, A123
- Dessauges-Zavadsky, M., Ginolfi, M., Pozzi, F., et al. 2020, *A&A*, 643, A5
- Dickinson, M., Giavalisco, M., & GOODS Team 2003, in *The Mass of Galaxies at Low and High Redshift*, eds. R. Bender, & A. Renzini, 324
- Donevski, D., Lapi, A., Małek, K., et al. 2020, *A&A*, 644, A144
- Donley, J. L., Rieke, G. H., Rigby, J. R., & Pérez-González, P. G. 2005, *ApJ*, 634, 169
- Draine, B. T., & Li, A. 2007, *ApJ*, 657, 810
- Draine, B. T., Dale, D. A., Bendo, G., et al. 2007, *ApJ*, 663, 866
- Draine, B. T., Aniano, G., Krause, O., et al. 2014, *ApJ*, 780, 172
- Elbaz, D., Daddi, E., Le Borgne, D., et al. 2007, *A&A*, 468, 33
- Elbaz, D., Dickinson, M., Hwang, H. S., et al. 2011, *A&A*, 533, A119
- Elbaz, D., Leiton, R., Nagar, N., et al. 2018, *A&A*, 616, A110
- Elmegreen, B. G., Bournaud, F., & Elmegreen, D. M. 2008, *ApJ*, 688, 67
- Erb, D. K., Shapley, A. E., Pettini, M., et al. 2006, *ApJ*, 644, 813
- Erben, T., Schirmer, M., Dietrich, J. P., et al. 2005, *Astron. Nachr.*, 326, 432
- Feldmann, R., & Mayer, L. 2015, *MNRAS*, 446, 1939
- Fontana, A., Dunlop, J. S., Paris, D., et al. 2014, *A&A*, 570, A11
- Franco, M., Elbaz, D., Béthermin, M., et al. 2018, *A&A*, 620, A152
- Franco, M., Elbaz, D., Zhou, L., et al. 2020a, *A&A*, 643, A30
- Franco, M., Elbaz, D., Zhou, L., et al. 2020b, *A&A*, 643, A53
- Fujimoto, S., Ouchi, M., Shibuya, T., & Nagai, H. 2017, *ApJ*, 850, 83
- Fujimoto, S., Ouchi, M., Kohno, K., et al. 2018, *ApJ*, 861, 7
- Garilli, B., McLure, R., Pentericci, L., et al. 2021, *A&A*, 647, A150
- Genzel, R., Tacconi, L. J., Gracia-Carpio, J., et al. 2010, *MNRAS*, 407, 2091
- Genzel, R., Tacconi, L. J., Lutz, D., et al. 2015, *ApJ*, 800, 20
- Giavalisco, M., Ferguson, H. C., Koekemoer, A. M., et al. 2004, *ApJ*, 600, L93
- Gómez-Guijarro, C., Toft, S., Karim, A., et al. 2018, *ApJ*, 856, 121
- Gómez-Guijarro, C., Magdis, G. E., Valentino, F., et al. 2019, *ApJ*, 886, 88
- Gómez-Guijarro, C., Elbaz, D., Xiao, M., et al. 2022, *A&A*, 658, A43
- González-López, J., Decarli, R., Pavesi, R., et al. 2019, *ApJ*, 882, 139
- Gordon, K. D., Galliano, F., Hony, S., et al. 2010, *A&A*, 518, L89
- Grogin, N. A., Kocevski, D. D., Faber, S. M., et al. 2011, *ApJS*, 197, 35
- Groves, B. A., Schinnerer, E., Leroy, A., et al. 2015, *ApJ*, 799, 96
- Gullberg, B., Smail, I., Swinbank, A. M., et al. 2019, *MNRAS*, 490, 4956
- Harrington, K. C., Weiss, A., Yun, M. S., et al. 2021, *ApJ*, 908, 95
- Heckman, T. M. 2005, in *Local Starbursts in a Cosmological Context*, eds. R. de Grijs, & R. M. González Delgado, 329, 3
- Helou, G., Soifer, B. T., & Rowan-Robinson, M. 1985, *ApJ*, 298, L7
- Herenz, E. C., Urrutia, T., Wisotzki, L., et al. 2017, *A&A*, 606, A12
- Hildebrand, R. H. 1983, *Q. J. R. Astron. Soc.*, 24, 267
- Hildebrandt, H., Erben, T., Dietrich, J. P., et al. 2006, *A&A*, 452, 1121
- Hodge, J. A., & da Cunha, E. 2020, *R. Soc. Open Sci.*, 7, 200556
- Hodge, J. A., Swinbank, A. M., Simpson, J. M., et al. 2016, *ApJ*, 833, 103
- Hopkins, P. F., Hernquist, L., Cox, T. J., et al. 2006, *ApJS*, 163, 1
- Hsieh, B.-C., Wang, W.-H., Hsieh, C.-C., et al. 2012, *ApJS*, 203, 23
- Hwang, H. S., Elbaz, D., Magdis, G., et al. 2010, *MNRAS*, 409, 75
- Ikarashi, S., Ivison, R. J., Caputi, K. I., et al. 2015, *ApJ*, 810, 133
- Illingworth, G., Magee, D., Bouwens, R., et al. 2016, *ArXiv e-prints* [arXiv:1606.00841]
- Jiménez-Andrade, E. F., Magnelli, B., Karim, A., et al. 2019, *A&A*, 625, A114
- Jiménez-Andrade, E. F., Murphy, E. J., Heywood, I., et al. 2021, *ApJ*, 910, 106
- Jin, S., Daddi, E., Liu, D., et al. 2018, *ApJ*, 864, 56
- Jin, S., Daddi, E., Magdis, G. E., et al. 2019, *ApJ*, 887, 144
- Joseph, R. D., & Wright, G. S. 1985, *MNRAS*, 214, 87
- Kartaltepe, J. S., Dickinson, M., Alexander, D. M., et al. 2012, *ApJ*, 757, 23
- Kauffmann, G., Heckman, T. M., Tremonti, C., et al. 2003, *MNRAS*, 346, 1055
- Kellermann, K. I., & Pauliny-Toth, I. I. K. 1969, *ApJ*, 155, L71
- Kennicutt, R. C., Jr. 1998, *ARA&A*, 36, 189
- Kewley, L. J., & Dopita, M. A. 2002, *ApJS*, 142, 35
- Kewley, L. J., & Ellison, S. L. 2008, *ApJ*, 681, 1183
- Kewley, L. J., Dopita, M. A., Leitherer, C., et al. 2013, *ApJ*, 774, 100
- Koekemoer, A. M., Faber, S. M., Ferguson, H. C., et al. 2011, *ApJS*, 197, 36
- Kokorev, V. I., Magdis, G. E., Davidzon, I., et al. 2021, *ApJ*, 921, 40
- Kovács, A., Chapman, S. C., Dowell, C. D., et al. 2006, *ApJ*, 650, 592
- Kriek, M., van Dokkum, P. G., Labbé, I., et al. 2009, *ApJ*, 700, 221
- Labbé, I., Oesch, P. A., Illingworth, G. D., et al. 2015, *ApJS*, 221, 23
- Lang, P., Schinnerer, E., Smail, I., et al. 2019, *ApJ*, 879, 54
- Lehnert, M. D., Le Tiran, L., Nesvadba, N. P. H., et al. 2013, *A&A*, 555, A72
- Leiton, R., Elbaz, D., Okumura, K., et al. 2015, *A&A*, 579, A93
- Leroy, A. K., Bolatto, A., Gordon, K., et al. 2011, *ApJ*, 737, 12
- Leslie, S. K., Schinnerer, E., Liu, D., et al. 2020, *ApJ*, 899, 58

- Liu, D., Daddi, E., Dickinson, M., et al. 2018, *ApJ*, 853, 172
- Liu, D., Schinnerer, E., Groves, B., et al. 2019, *ApJ*, 887, 235
- Luo, B., Brandt, W. N., Xue, Y. Q., et al. 2017, *ApJS*, 228, 2
- Lutz, D., Poglitsch, A., Altieri, B., et al. 2011, *A&A*, 532, A90
- Madau, P., & Dickinson, M. 2014, *ARA&A*, 52, 415
- Magdis, G. E., Daddi, E., Elbaz, D., et al. 2011, *ApJ*, 740, L15
- Magdis, G. E., Daddi, E., Béthermin, M., et al. 2012, *ApJ*, 760, 6
- Magdis, G. E., Rigopoulou, D., Daddi, E., et al. 2017, *A&A*, 603, A93
- Magnelli, B., Lutz, D., Santini, P., et al. 2012, *A&A*, 539, A155
- Magnelli, B., Popesso, P., Berta, S., et al. 2013, *A&A*, 553, A132
- Magnelli, B., Lutz, D., Saintonge, A., et al. 2014, *A&A*, 561, A86
- Magnelli, B., Boogaard, L., Decarli, R., et al. 2020, *ApJ*, 892, 66
- Mannucci, F., Cresci, G., Maiolino, R., Marconi, A., & Gnerucci, A. 2010, *MNRAS*, 408, 2115
- McMullin, J. P., Waters, B., Schiebel, D., Young, W., & Golap, K. 2007, in *Astronomical Data Analysis Software and Systems XVI*, eds. R. A. Shaw, F. Hill, & D. J. Bell, *ASP Conf. Ser.*, 376, 127
- Mihos, J. C., & Hernquist, L. 1996, *ApJ*, 464, 641
- Mineo, S., Gilfanov, M., & Sunyaev, R. 2012, *MNRAS*, 419, 2095
- Mowla, L. A., van Dokkum, P., Brammer, G. B., et al. 2019, *ApJ*, 880, 57
- Mullaney, J. R., Alexander, D. M., Goulding, A. D., & Hickox, R. C. 2011, *MNRAS*, 414, 1082
- Murphy, E. J., Momjian, E., Condon, J. J., et al. 2017, *ApJ*, 839, 35
- Nelson, E., van Dokkum, P., Franx, M., et al. 2014, *Nature*, 513, 394
- Noeske, K. G., Weiner, B. J., Faber, S. M., et al. 2007, *ApJ*, 660, L43
- Nonino, M., Dickinson, M., Rosati, P., et al. 2009, *ApJS*, 183, 244
- Obreschkow, D., & Rawlings, S. 2009, *ApJ*, 696, L129
- Oke, J. B. 1974, *ApJS*, 27, 21
- Oliver, S. J., Bock, J., Altieri, B., et al. 2012, *MNRAS*, 424, 1614
- Ostriker, E. C., & Shetty, R. 2011, *ApJ*, 731, 41
- Peng, C. Y., Ho, L. C., Impey, C. D., & Rix, H.-W. 2002, *AJ*, 124, 266
- Pettini, M., & Pagel, B. E. J. 2004, *MNRAS*, 348, L59
- Puglisi, A., Daddi, E., Liu, D., et al. 2019, *ApJ*, 877, L23
- Puglisi, A., Daddi, E., Valentino, F., et al. 2021, *MNRAS*, 508, 5217
- Reddy, N. A., Steidel, C. C., Erb, D. K., Shapley, A. E., & Pettini, M. 2006, *ApJ*, 653, 1004
- Rees, M. J., & Ostriker, J. P. 1977, *MNRAS*, 179, 541
- Rémy-Ruyer, A., Madden, S. C., Galliano, F., et al. 2014, *A&A*, 563, A31
- Retzlaff, J., Rosati, P., Dickinson, M., et al. 2010, *A&A*, 511, A50
- Riechers, D. A., Pavesi, R., Sharon, C. E., et al. 2019, *ApJ*, 872, 7
- Rujopakarn, W., Dunlop, J. S., Rieke, G. H., et al. 2016, *ApJ*, 833, 12
- Rujopakarn, W., Daddi, E., Rieke, G. H., et al. 2019, *ApJ*, 882, 107
- Salpeter, E. E. 1955, *ApJ*, 121, 161
- Santini, P., Fontana, A., Grazian, A., et al. 2012, *A&A*, 538, A33
- Schinnerer, E., Groves, B., Sargent, M. T., et al. 2016, *ApJ*, 833, 112
- Schreiber, C., Pannella, M., Elbaz, D., et al. 2015, *A&A*, 575, A74
- Schreiber, C., Elbaz, D., Pannella, M., et al. 2016, *A&A*, 589, A35
- Schreiber, C., Elbaz, D., Pannella, M., et al. 2018, *A&A*, 609, A30
- Scoville, N., Aussel, H., Sheth, K., et al. 2014, *ApJ*, 783, 84
- Scoville, N., Sheth, K., Aussel, H., et al. 2016, *ApJ*, 820, 83
- Scoville, N., Lee, N., Vanden Bout, P., et al. 2017, *ApJ*, 837, 150
- Shen, S., Mo, H. J., White, S. D. M., et al. 2003, *MNRAS*, 343, 978
- Simpson, J. M., Smail, I., Swinbank, A. M., et al. 2015, *ApJ*, 799, 81
- Speagle, J. S., Steinhardt, C. L., Capak, P. L., & Silverman, J. D. 2014, *ApJS*, 214, 15
- Steidel, C. C., Rudie, G. C., Strom, A. L., et al. 2014, *ApJ*, 795, 165
- Straatman, C. M. S., Labbé, I., Spitler, L. R., et al. 2015, *ApJ*, 808, L29
- Straatman, C. M. S., Spitler, L. R., Quadri, R. F., et al. 2016, *ApJ*, 830, 51
- Suess, K. A., Kriek, M., Price, S. H., & Barro, G. 2019, *ApJ*, 877, 103
- Suess, K. A., Kriek, M., Price, S. H., & Barro, G. 2021, *ApJ*, 915, 87
- Tacchella, S., Dekel, A., Carollo, C. M., et al. 2016, *MNRAS*, 457, 2790
- Tacconi, L. J., Genzel, R., Neri, R., et al. 2010, *Nature*, 463, 781
- Tacconi, L. J., Genzel, R., Saintonge, A., et al. 2018, *ApJ*, 853, 179
- Tan, Q., Daddi, E., Sargent, M., et al. 2013, *ApJ*, 776, L24
- Toft, S., Smolčić, V., Magnelli, B., et al. 2014, *ApJ*, 782, 68
- Urrutia, T., Wisotzki, L., Kerutt, J., et al. 2019, *A&A*, 624, A141
- Valentino, F., Daddi, E., Puglisi, A., et al. 2021, *A&A*, 654, A165
- van der Wel, A., Franx, M., van Dokkum, P. G., et al. 2014, *ApJ*, 788, 28
- van Dokkum, P. G., Nelson, E. J., Franx, M., et al. 2015, *ApJ*, 813, 23
- Whitaker, K. E., van Dokkum, P. G., Brammer, G., & Franx, M. 2012, *ApJ*, 754, L29
- Whitaker, K. E., Bezanson, R., van Dokkum, P. G., et al. 2017, *ApJ*, 838, 19
- Whitaker, K. E., Ashas, M., Illingworth, G., et al. 2019, *ApJS*, 244, 16
- Williams, C. C., Giavalisco, M., Cassata, P., et al. 2014, *ApJ*, 780, 1
- Windhorst, R. A., Cohen, S. H., Hathi, N. P., et al. 2011, *ApJS*, 193, 27
- Wuyts, S., Labbé, I., Förster Schreiber, N. M., et al. 2008, *ApJ*, 682, 985
- Zhou, L., Elbaz, D., Franco, M., et al. 2020, *A&A*, 642, A155
- Zolotov, A., Dekel, A., Mandelker, N., et al. 2015, *MNRAS*, 450, 2327
-
- ¹ AIM, CEA, CNRS, Université Paris-Saclay, Université Paris Diderot, Sorbonne Paris Cité, 91191 Gif-sur-Yvette, France
e-mail: carlos.gomezguijarro@cea.fr
- ² School of Astronomy and Space Science, Nanjing University, Nanjing 210093, PR China
- ³ Cosmic Dawn Center (DAWN), Denmark
- ⁴ Niels Bohr Institute, University of Copenhagen, Jagtvej 128, 2200 Copenhagen N, Denmark
- ⁵ DTU-Space, Technical University of Denmark, Elektrovej 327, 2800 Kgs. Lyngby, Denmark
- ⁶ Astronomy Centre, Department of Physics and Astronomy, University of Sussex, Brighton BN1 9QH, UK
- ⁷ International Space Science Institute (ISSI), Hallerstrasse 6, 3012 Bern, Switzerland
- ⁸ Community Science and Data Center/NSF's NOIRLab., 950 N. Cherry Ave., Tucson, AZ 85719, USA
- ⁹ Aix Marseille Université, CNRS, LAM, Laboratoire d'Astrophysique de Marseille, Marseille, France
- ¹⁰ Centre for Astrophysics Research, University of Hertfordshire, Hatfield AL10 9AB, UK
- ¹¹ Astronomy Department, University of Massachusetts, Amherst, MA 01003, USA
- ¹² Departamento de Astronomía, Facultad de Ciencias Físicas y Matemáticas, Universidad de Concepción, Concepción, Chile
- ¹³ Hiroshima Astrophysical Science Center, Hiroshima University, 1-3-1 Kagamiyama, Higashi-Hiroshima, Hiroshima 739-8526, Japan
- ¹⁴ Department of Physics, Faculty of Science, Chulalongkorn University, 254 Phayathai Road, Pathumwan, Bangkok 10330, Thailand
- ¹⁵ National Astronomical Research Institute of Thailand (Public Organization), Don Kaeo, Mae Rim, Chiang Mai 50180, Thailand
- ¹⁶ Kavli IPMU (WPI), UTIAS, The University of Tokyo, Kashiwa, Chiba 277-8583, Japan
- ¹⁷ Department of Physics, Anhui Normal University, Wuhu, Anhui 241000, PR China
- ¹⁸ Key Laboratory of Modern Astronomy and Astrophysics (Nanjing University), Ministry of Education, Nanjing 210093, PR China
- ¹⁹ Centre for Extragalactic Astronomy, Department of Physics, Durham University, Durham DH1 3LE, UK
- ²⁰ Infrared Processing and Analysis Center, MS314-6, California Institute of Technology, Pasadena, CA 91125, USA
- ²¹ Space Telescope Science Institute, 3700 San Martin Drive, Baltimore, MD 21218, USA
- ²² Department of Astronomy, The University of Texas at Austin, Austin, TX 78712, USA
- ²³ National Astronomical Observatory of Japan, National Institutes of Natural Sciences, 2-21-1 Osawa, Mitaka, Tokyo 181-8588, Japan
- ²⁴ SOKENDAI (The Graduate University for Advanced Studies), 2-21-1 Osawa, Mitaka, Tokyo 181-8588, Japan
- ²⁵ School of Physics and Astronomy, Rochester Institute of Technology, 84 Lomb Memorial Drive, Rochester, NY 14623, USA
- ²⁶ Institute of Astronomy & Astrophysics, Academia Sinica, Taipei 10617, Taiwan
- ²⁷ Institute of Astronomy, Graduate School of Science, The University of Tokyo, 2-21-1 Osawa, Mitaka, Tokyo 181-0015, Japan
- ²⁸ Department of Physics and Astronomy, University of Sheffield, Sheffield S3 7RH, UK
- ²⁹ Astronomy Unit, Department of Physics, University of Trieste, Via Tiepolo 11, 34131 Trieste, Italy
- ³⁰ Fakultät für Physik der Ludwig-Maximilians-Universität, 81679 München, Germany
- ³¹ Department of Physics and Astronomy, Texas A&M University, College Station, TX 77843-4242, USA
- ³² George P. and Cynthia Woods Mitchell Institute for Fundamental Physics and Astronomy, Texas A&M University, College Station, TX 77843-4242, USA
- ³³ Instituto de Astrofísica, Facultad de Física, Pontificia Universidad Católica de Chile, Casilla 306, Santiago 22, Chile

Appendix A: Infrared SED fits

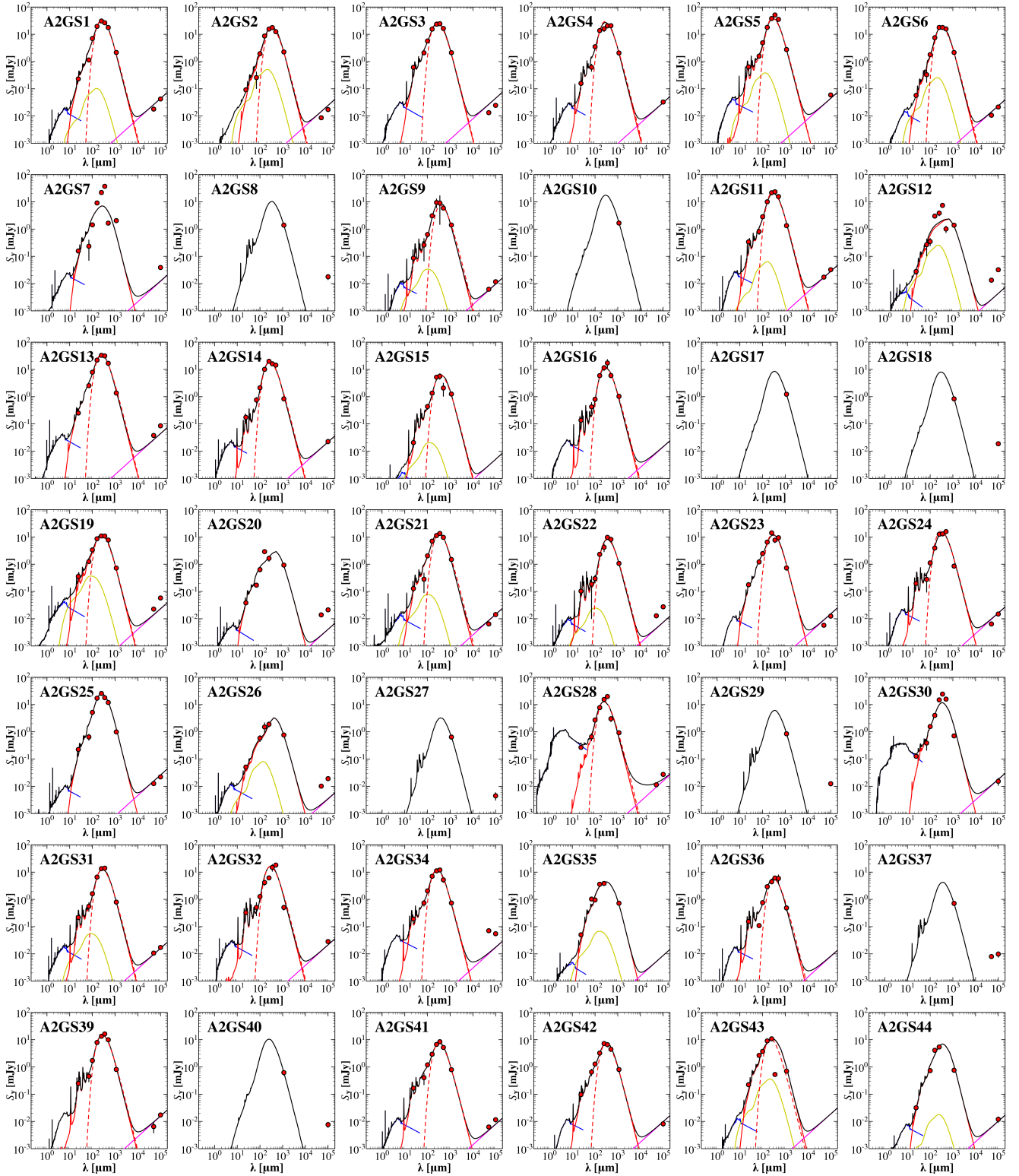


Fig. A.1. Mid-IR to mm SEDs for the galaxy sample. A2GS1 to A2GS44 correspond to the 100% pure source catalog in [Gómez-Guijarro et al. \(2022\)](#). *Herschel*-detected galaxies were fit with the code *Stardust* accounting for the stellar emission (blue), AGN contribution (yellow), dust emission from star formation (red), and radio emission (magenta). MBB fit is shown in dashed red. The galaxies without *Herschel* counterpart were fit following an iterative approach with the dust SED libraries by [Schreiber et al. \(2018\)](#) (see Sect. 3.2).

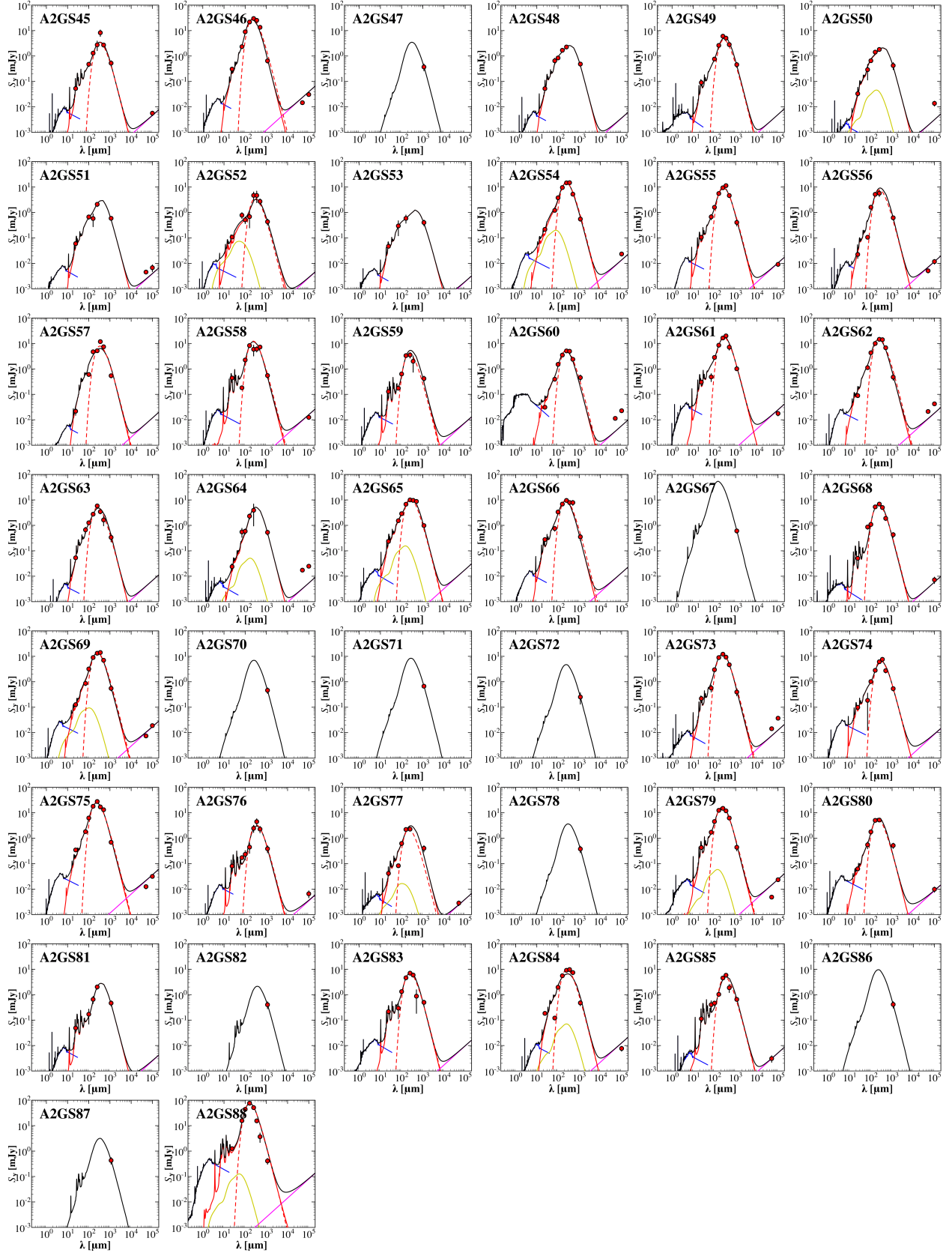


Fig. A.2. Mid-IR to mm SEDs for the galaxy sample as in Fig. A.1. A2GS45 to A2GS88 correspond to the prior-based source catalog in Gómez-Guijarro et al. (2022).

Appendix B: Infrared flux predictions

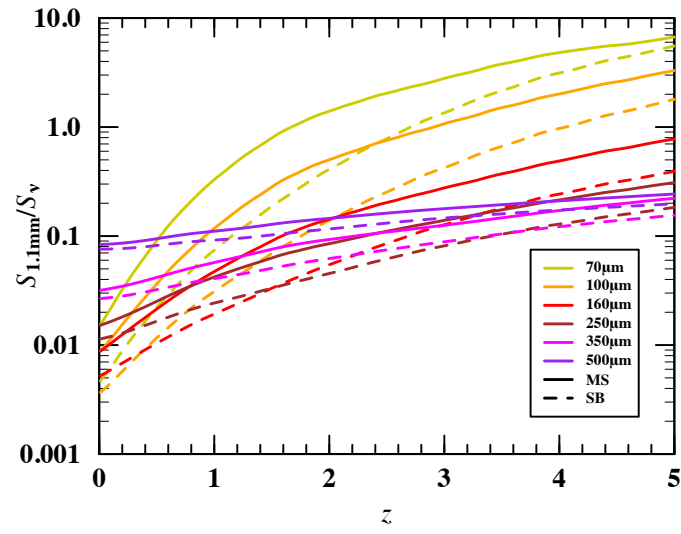


Fig. B.1. Predictions of flux ratios between ALMA 1.1 mm and *Herschel* PACS (70, 100, 160 μm) and SPIRE (250, 350, 500 μm) bands as a function of redshift for both MS ($\Delta\text{MS} = 1$) and SB ($\Delta\text{MS} = 5$) templates. See Table B.1 for these flux ratio predictions tabulated.

Table B.1. Flux ratios between ALMA 1.1 mm and *Herschel* bands for a MS (SB) template as a function of redshift.

z	$S_{1.1\text{mm}}/S_{70\mu\text{m}}$	$S_{1.1\text{mm}}/S_{100\mu\text{m}}$	$S_{1.1\text{mm}}/S_{160\mu\text{m}}$	$S_{1.1\text{mm}}/S_{250\mu\text{m}}$	$S_{1.1\text{mm}}/S_{350\mu\text{m}}$	$S_{1.1\text{mm}}/S_{500\mu\text{m}}$
0.1	0.0214 (0.0065)	0.0112 (0.0046)	0.0103 (0.0060)	0.0164 (0.0121)	0.0329 (0.0274)	0.0844 (0.0763)
0.2	0.0322 (0.0089)	0.0154 (0.0058)	0.0125 (0.0069)	0.0181 (0.0129)	0.0347 (0.0282)	0.0862 (0.0769)
0.3	0.0472 (0.0119)	0.0208 (0.0072)	0.0150 (0.0078)	0.0202 (0.0138)	0.0367 (0.0292)	0.0884 (0.0779)
0.4	0.0676 (0.0169)	0.0282 (0.0094)	0.0182 (0.0092)	0.0227 (0.0152)	0.0393 (0.0308)	0.0915 (0.0800)
0.5	0.0877 (0.0222)	0.0354 (0.0117)	0.0210 (0.0104)	0.0249 (0.0166)	0.0415 (0.0323)	0.0942 (0.0821)
0.6	0.1207 (0.0286)	0.0467 (0.0143)	0.0251 (0.0118)	0.0280 (0.0179)	0.0444 (0.0338)	0.0978 (0.0842)
0.7	0.1622 (0.0364)	0.0610 (0.0174)	0.0301 (0.0134)	0.0315 (0.0195)	0.0478 (0.0355)	0.1018 (0.0865)
0.8	0.2125 (0.0481)	0.0781 (0.0217)	0.0356 (0.0153)	0.0352 (0.0212)	0.0512 (0.0375)	0.1055 (0.0888)
0.9	0.2707 (0.0626)	0.0977 (0.0268)	0.0415 (0.0175)	0.0388 (0.0230)	0.0544 (0.0393)	0.1084 (0.0906)
1.0	0.3408 (0.0755)	0.1215 (0.0314)	0.0482 (0.0195)	0.0425 (0.0245)	0.0576 (0.0409)	0.1112 (0.0921)
1.1	0.3943 (0.0898)	0.1402 (0.0363)	0.0536 (0.0214)	0.0456 (0.0258)	0.0603 (0.0423)	0.1135 (0.0933)
1.2	0.4795 (0.1125)	0.1692 (0.0439)	0.0613 (0.0242)	0.0494 (0.0276)	0.0637 (0.0443)	0.1164 (0.0953)
1.3	0.5809 (0.1312)	0.2046 (0.0506)	0.0704 (0.0268)	0.0538 (0.0294)	0.0675 (0.0463)	0.1200 (0.0974)
1.4	0.6952 (0.1524)	0.2461 (0.0576)	0.0813 (0.0292)	0.0590 (0.0308)	0.0721 (0.0480)	0.1244 (0.0993)
1.5	0.7745 (0.1864)	0.2746 (0.0689)	0.0885 (0.0330)	0.0622 (0.0332)	0.0750 (0.0505)	0.1274 (0.1024)
1.6	0.9146 (0.2257)	0.3257 (0.0819)	0.1009 (0.0374)	0.0676 (0.0358)	0.0796 (0.0533)	0.1319 (0.1056)
1.7	1.0020 (0.2560)	0.3574 (0.0919)	0.1091 (0.0407)	0.0711 (0.0377)	0.0827 (0.0553)	0.1350 (0.1080)
1.8	1.1623 (0.3050)	0.4149 (0.1071)	0.1223 (0.0452)	0.0766 (0.0402)	0.0869 (0.0577)	0.1391 (0.1109)
1.9	1.2595 (0.3612)	0.4504 (0.1246)	0.1309 (0.0503)	0.0802 (0.0429)	0.0896 (0.0601)	0.1419 (0.1137)
2.0	1.3622 (0.4014)	0.4869 (0.1371)	0.1395 (0.0540)	0.0839 (0.0451)	0.0921 (0.0619)	0.1445 (0.1159)
2.1	1.5330 (0.4675)	0.5522 (0.1576)	0.1544 (0.0598)	0.0900 (0.0482)	0.0962 (0.0645)	0.1485 (0.1190)
2.2	1.6287 (0.5422)	0.5885 (0.1804)	0.1636 (0.0660)	0.0942 (0.0516)	0.0989 (0.0672)	0.1517 (0.1223)
2.3	1.7244 (0.6267)	0.6255 (0.2059)	0.1722 (0.0727)	0.0979 (0.0551)	0.1011 (0.0698)	0.1543 (0.1254)
2.4	1.9218 (0.6836)	0.7047 (0.2231)	0.1901 (0.0775)	0.1051 (0.0577)	0.1054 (0.0717)	0.1586 (0.1279)
2.5	2.0105 (0.7789)	0.7410 (0.2521)	0.2000 (0.0852)	0.1097 (0.0617)	0.1083 (0.0746)	0.1618 (0.1314)
2.6	2.2131 (0.8860)	0.8266 (0.2843)	0.2197 (0.0933)	0.1175 (0.0656)	0.1130 (0.0775)	0.1664 (0.1347)
2.7	2.3127 (1.0014)	0.8693 (0.3185)	0.2294 (0.1018)	0.1212 (0.0698)	0.1149 (0.0804)	0.1685 (0.1380)
2.8	2.3925 (1.1285)	0.9038 (0.3574)	0.2397 (0.1112)	0.1259 (0.0741)	0.1179 (0.0834)	0.1715 (0.1412)
2.9	2.6165 (1.2073)	0.9971 (0.3803)	0.2596 (0.1169)	0.1332 (0.0768)	0.1222 (0.0853)	0.1754 (0.1432)
3.0	2.8484 (1.3432)	1.0964 (0.4210)	0.2820 (0.1265)	0.1415 (0.0812)	0.1270 (0.0885)	0.1795 (0.1463)
3.1	2.9566 (1.5005)	1.1395 (0.4683)	0.2916 (0.1373)	0.1452 (0.0859)	0.1293 (0.0918)	0.1812 (0.1494)
3.2	3.1958 (1.6649)	1.2412 (0.5174)	0.3147 (0.1480)	0.1538 (0.0904)	0.1345 (0.0950)	0.1853 (0.1522)
3.3	3.2979 (1.8409)	1.2844 (0.5708)	0.3236 (0.1596)	0.1570 (0.0953)	0.1366 (0.0984)	0.1867 (0.1550)
3.4	3.5444 (2.0242)	1.3964 (0.6260)	0.3482 (0.1716)	0.1655 (0.1003)	0.1417 (0.1019)	0.1902 (0.1578)
3.5	3.8083 (2.1329)	1.5140 (0.6580)	0.3727 (0.1785)	0.1740 (0.1033)	0.1469 (0.1042)	0.1939 (0.1596)
3.6	3.8906 (2.3364)	1.5527 (0.7207)	0.3840 (0.1919)	0.1788 (0.1089)	0.1502 (0.1082)	0.1962 (0.1628)
3.7	4.1455 (2.5523)	1.6728 (0.7873)	0.4108 (0.2057)	0.1881 (0.1144)	0.1558 (0.1121)	0.2001 (0.1658)
3.8	4.4072 (2.7798)	1.8005 (0.8593)	0.4391 (0.2203)	0.1974 (0.1200)	0.1612 (0.1160)	0.2037 (0.1688)
3.9	4.6629 (3.0191)	1.9278 (0.9356)	0.4684 (0.2352)	0.2073 (0.1255)	0.1670 (0.1195)	0.2075 (0.1713)
4.0	4.7213 (3.1304)	1.9610 (0.9686)	0.4775 (0.2425)	0.2111 (0.1287)	0.1697 (0.1220)	0.2092 (0.1732)
4.1	4.9384 (3.3752)	2.0904 (1.0503)	0.5069 (0.2592)	0.2206 (0.1351)	0.1751 (0.1262)	0.2126 (0.1763)
4.2	5.1402 (3.4927)	2.2222 (1.0856)	0.5365 (0.2650)	0.2304 (0.1372)	0.1807 (0.1276)	0.2163 (0.1772)
4.3	5.3284 (3.7507)	2.3636 (1.1726)	0.5696 (0.2813)	0.2411 (0.1431)	0.1864 (0.1313)	0.2200 (0.1799)
4.4	5.5201 (4.0051)	2.5058 (1.2588)	0.6019 (0.2972)	0.2515 (0.1488)	0.1919 (0.1348)	0.2234 (0.1824)
4.5	5.7285 (4.2821)	2.6485 (1.3540)	0.6354 (0.3156)	0.2629 (0.1557)	0.1982 (0.1391)	0.2276 (0.1857)
4.6	5.7424 (4.4140)	2.6869 (1.3974)	0.6430 (0.3234)	0.2660 (0.1589)	0.2002 (0.1412)	0.2290 (0.1874)
4.7	5.9467 (4.7096)	2.8400 (1.4997)	0.6766 (0.3413)	0.2766 (0.1653)	0.2057 (0.1451)	0.2326 (0.1903)
4.8	6.1782 (4.9964)	2.9968 (1.6030)	0.7115 (0.3601)	0.2878 (0.1719)	0.2113 (0.1489)	0.2361 (0.1931)
4.9	6.4334 (5.3042)	3.1509 (1.7130)	0.7450 (0.3788)	0.2987 (0.1783)	0.2168 (0.1525)	0.2396 (0.1956)
5.0	6.7310 (5.4396)	3.3228 (1.7577)	0.7834 (0.3858)	0.3110 (0.1811)	0.2230 (0.1542)	0.2436 (0.1970)

Appendix C: Impact of metallicity assumptions

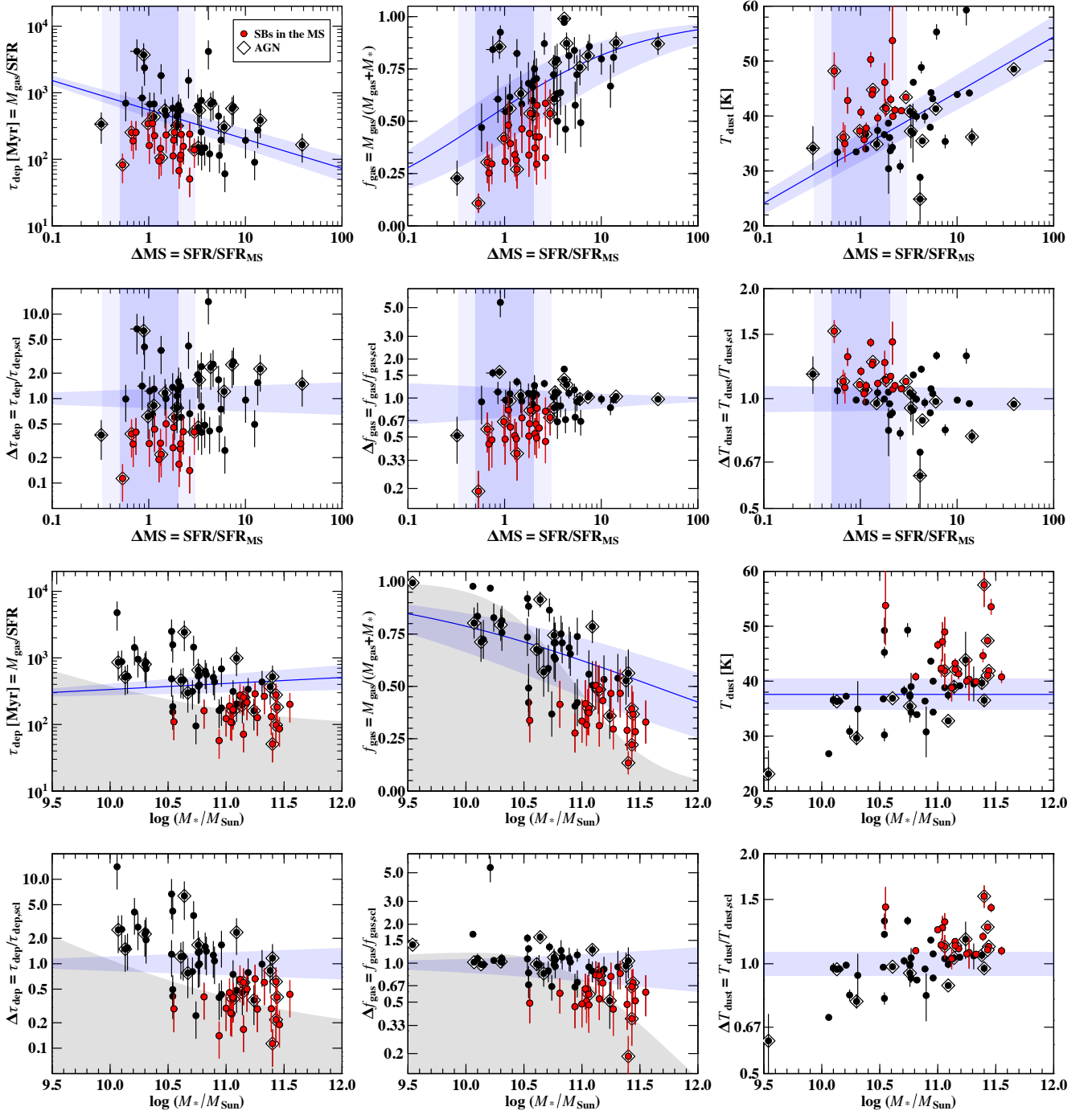


Fig. C.1. Same as Fig 3, but where M_{gas} estimates were obtained by using the $\delta_{\text{GDR-Z}}$ with FMR instead of MZR. We note that as T_{dust} estimates are independent of the metallicity assumption, the third column remains unchanged. The subset of SBs in the MS highlighted in red is the same as in Fig 3 selected from MZR.

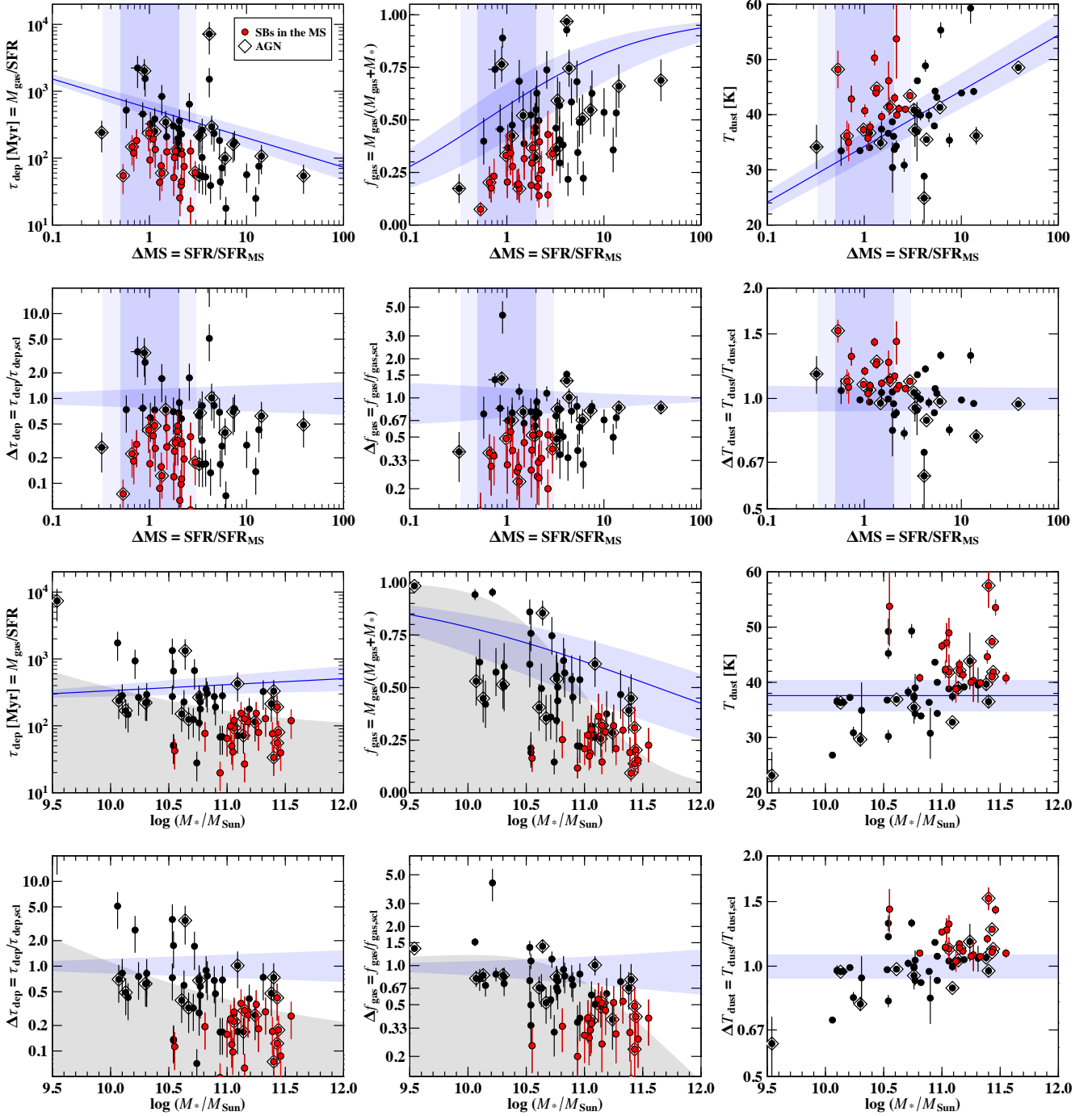


Fig. C.2. Same as Fig 3, but where M_{gas} estimates were obtained by using the $\delta_{GDR}-Z$ with fixed solar metallicity instead of MZR. We note that as T_{dust} estimates are independent of the metallicity assumption, the third column remains unchanged. The subset of SBs in the MS highlighted in red is the same as in Fig 3 selected from MZR.

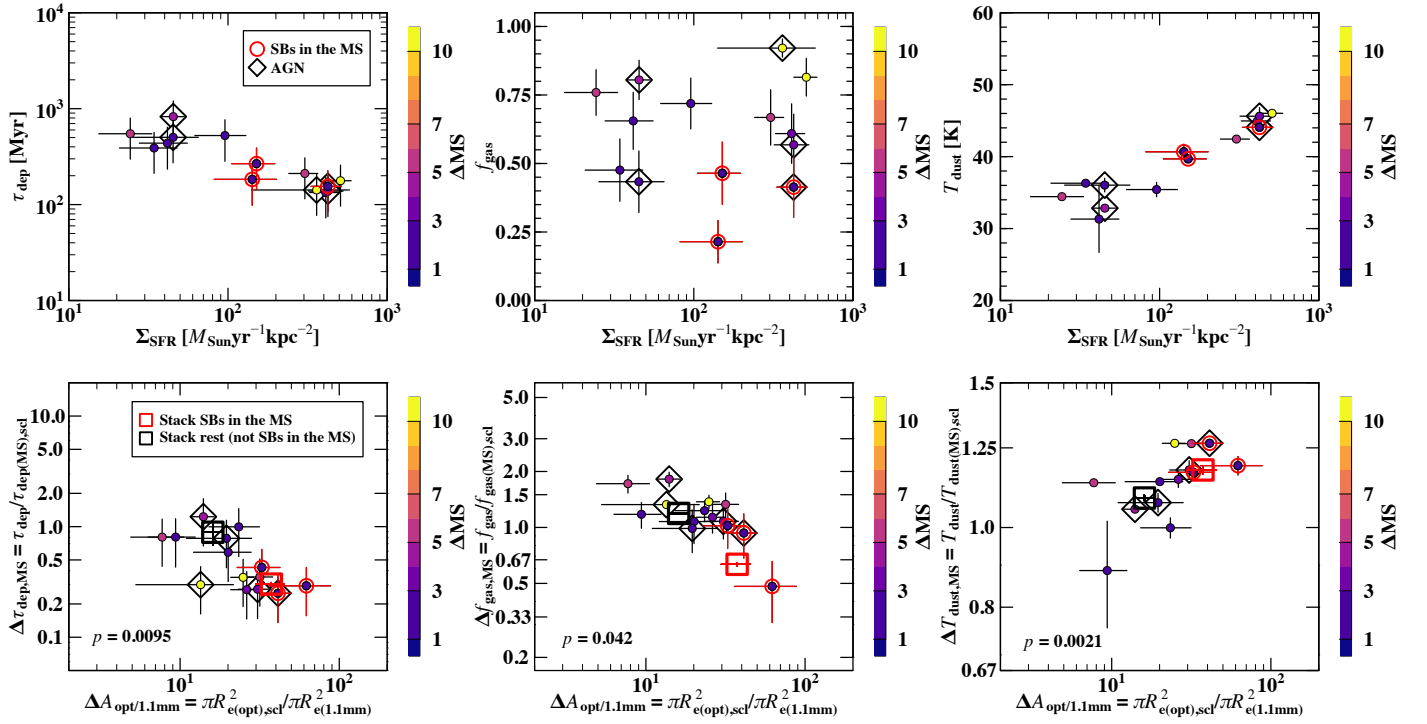


Fig. C.3. Same as Fig 4, but where M_{gas} estimates were obtained by using the $\delta_{\text{GDR}}-Z$ with FMR instead of MZR. We note that as T_{dust} estimates are independent of the metallicity assumption, the third column remains unchanged. The subset of SBs in the MS highlighted in red is the same as in Fig 3 selected from MZR.

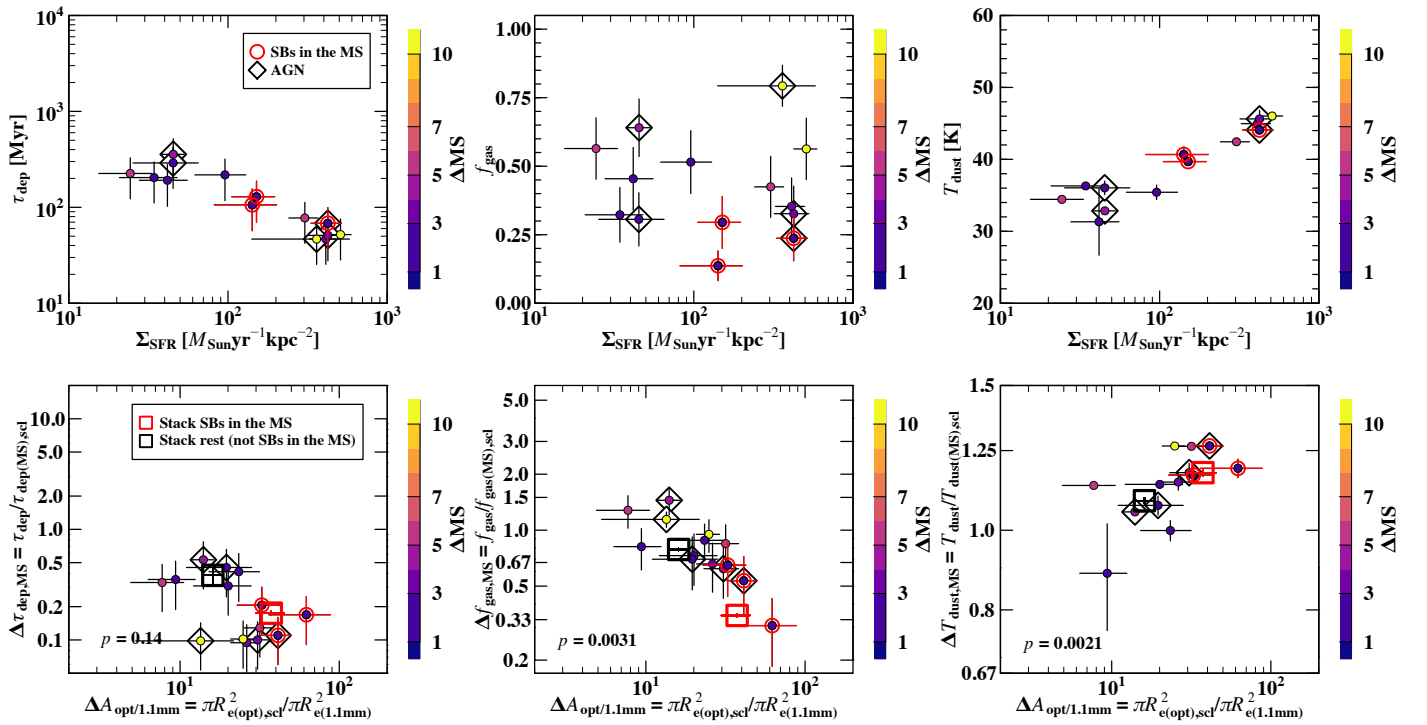


Fig. C.4. Same as Fig 4, but where M_{gas} estimates were obtained by using the $\delta_{\text{GDR}}-Z$ with fixed solar metallicity instead of MZR. We note that as T_{dust} estimates are independent of the metallicity assumption, the third column remains unchanged. The subset of SBs in the MS highlighted in red is the same as in Fig 3 selected from MZR.